Unsteady RANS Simulation of Turbulent Flow Over a Weapon-Bay Cavity

SHIA-HUI PENG

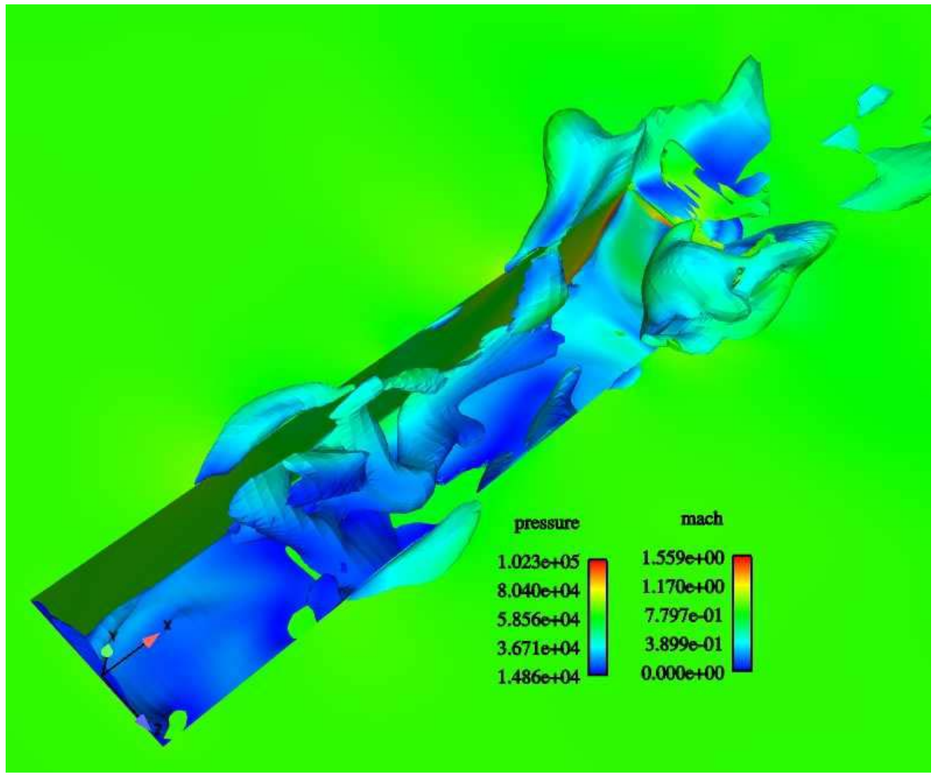

FOI
Defence Research Agency
Systems Technology
SE-164 90 Stockholm

Phone: +46 8 555 030 00
Fax: +46 8 555 031 00

www.foi.se

FOI-R--1983 --SE Scientific report
ISSN 1650-1942 May 2006

Systems Technology

Shia-Hui Peng

Unsteady RANS Simulation of Turbulent Flow Over a Weapon-Bay Cavity

FOI-R--1983--SE Scientific report **Systems Technology**
ISSN-1650-1942 May 2006

Issuing organisation FOI – Swedish Defence Research Agency Systems Technology SE-164 90 STOCKHOLM	**Report number, ISRN** FOI-R--1983--SE	**Report type** Scientific report
	Research area code 7. Vehicles	
	Month year May 2006	**Project no.** E61109
	Sub area code 5 5 . Air Vehicles	
	Sub area code 2 5 4 . Unmanned Vehicles	
Author/s (editor/s) Shia-Hui Peng	**Project manager** Staffan Meijer	
	Approved by Monica Dahlén Head, Systems Technology	
	Sponsoring agency FMV	
	Scientifically and technically responsible Peter Elliasson	

Report title
Unsteady RANS Simulation of Turbulent Flow Over a Weapon-Bay Cavity

Abstract
The unsteady turbulent flow over a weapon-bay cavity configuration was numerically investigated. The rectangular cavity has an aspect ratio of $5:1:1$, which is configured to model an embedded weapon-bay geometry of military aircraft in a freestream with a Mach number of $M_\infty = 0.85$. The turbulent cavity flow was modelled with the Spalart-Allmaras RANS model based on the unstructured CFD solver EDGE. The result was focused on the surface pressure fluctuations and resulting sound resonance from the cavity due to unsteady pressure oscillations, for which experiment was conducted by QinetiQ and had been used in this work for comparison. The RANS-computed flow features arising within the cavity were also analyzed, and the mean flow was compared with a well-resolved large eddy simulation. As compared with experimental data, the prediction of the pressure-induced tonal modes (for both the tonal frequency and magnitude) was significantly improved over previous 2D URANS computations. It was shown that the URANS simulation is able to produce reasonable simulations, in particular, for the amplitude of the second pressure mode and the frequency of the third mode in the analysis of the sound resonance radiated from the cavity. The predicted mean flow was shown in reasonable agreement with the LES data, but the velocity in the inner edge of the shear layer next to the recirculation was somewhat underestimated in the rear part of the cavity.

Keywords
RANS modelling, Unsteady weapon-bay cavity flow, Pressure fluctuations, Power spectral density (PSD), Sound pressure level (SPL), Mean cavity flow

Further bibliographic information	**Language** English
ISSN ISSN-1650-1942	**Pages** 34 p.
	Price acc. to pricelist

Utgivare FOI – Totalförsvarets forskningsinstitut Systemteknik 164 90 STOCKHOLM	**Rapportnummer, ISRN** FOI-R--1983--SE	**Klassificering** Vetenskaplig rapport
	Forskningsområde 7. Farkoster	
	Månad år Maj 2006	**Projektnummer** E61109
	Delområde 5 5 . Luftfarkoster	
	Delområde 2 5 4 . Obemannade farkoster	
Författare/redaktör Shia-Hui Peng	**Projektledare** Staffan Meijer	
	Godkänd av Monica Dahlén Chef, Systemteknik	
	Uppdragsgivare/kundbeteckning FMV	
	Tekniskt och/eller vetenskapligt ansvarig Peter Elliasson	

Rapportens titel
Instationär RANS Simulering av Turbulenta Strömning i ett Kavitetsformat Vapenschakt

Sammanfattning
Rapporten beskriver en numerisk undersökning av instationär strömning i en rektangulärt kavitet. Kaviteten har ett sidoförhällande på $5:1:1$ och undersökningen har för avsikt att modellera geometrin av ett typiskt vapenschakt i ett militärt flygplan som flyger vid ett Machtal av $M = 0.85$. Den turbulenta strömningen i kaviteten har modellerats med Spalart-Allmaras RANS turbulensmodell med strömningslösaren EDGE för ostrukturerade nät. Undersökningen fokuserar framförallt på fluktuationer av yttryck och ljudnivåer med jämförelser av experimentella data från QinetiQ. Strömningen i kaviteten har också analyserats och medelströmningen har jämförts med resultat från en väl upplöst Large Eddy Simulation (LES). Prediktionen av de utmärkande tryckinducerade ljudtonerna har avsevärt förbättrats, både vad gäller frekvens och amplitud, jämfört med tidigare motsvarande beräkningar i 2D. Det har visats att URANS simuleringen predikterar väl framförallt amplituden av 2:a moden och frekvensen för 3:e moden i analysen av ljudresonansen från kaviteten. Medelströmningen stämmer bra med LES data men hastigheten vid inre kanten av skärskiktet bredvid recirkulationen är något underpredikterad i bakre delen av kaviteten.

Nyckelord
RANS modellering, Instationär kavitetsströmming, Vapenschakt, Tryckfluktuationer, Effekttäthetsspektrum (PSD), Ljudtrycksnivå (SPL), Medelströmning i kaviteten

Övriga bibliografiska uppgifter	**Språk** Engelska
ISSN ISSN-1650-1942	**Antal sidor:** 34 s.
Distribution enligt missiv	**Pris: Enligt prislista**

Contents

1 Introduction

The flow over cavities is relevant to a wide variety of applications. Typical examples of cavities include gate slots, open windows in automobile industry, as well as depressions in submarine and ship hulls and gas dynamic laser cavities. Flow past configurations as such can be equivalently studied as cavity flows. In aeronautic and military-aircraft related applications, cavity flows can be observed around weapon bomb bays, landing gear housing and projectiles, as well as in-flight re-fuelling ports and pressure vents in the space shuttle's cargo bay. For cavities embedded in an aircraft, the flows over the weapon bay and the under-carriage wheel well are two typical examples of cavity flows that have received intensive attention by means of experimental and computational analysis. This is not only because such cavity flows may significantly affect the aircraft performance but also because they are of fundamental interest in research of turbulent flow physics.

The under-carriage wheel wells are considered being the primary noise source because of the deployment of the landing gear during landing approach and touchdown. The airframe-generated noise is one of the major concerns of noise propagated into the passenger cabin of the aircraft and radiated over surrounding populated area. Apart from the sound resonance generated by flow instabilities, weapon-bay type cavities have also been a noticeable topic in studies of modern military aircraft, where radar invisibility and high maneuverability are basic design criteria. To reduce the susceptibility to radar detection, the internal storage of missiles has been an enforced routine, which possesses also an additional advantage of diminishing the profile drag of the aircraft. Nonetheless, embedding the stores in cavities and releasing them at high speeds may cause problems associated with store separation and even with potential structural and store damages. Certainly, justification of such problems and of other undesirable flow scenarios is closely related to the aerodynamic flow properties around and in the embedded cavity. A typical example is the large nose-up pitching moments due to an adverse static pressure gradient in the cavity, which may cause catastrophic consequence for separating store. Additionally, the extensive pressure oscillations may cause premature structural fatigue and possible damages to the housed electrical equipment. The cavity, similar to a simplified embedded weapon bay, is the configuration to study in the present work.

Highly unsteady flow may be triggered over weapon bays when opened prior to in-flight deployment of the weapons. Such a flow is usually characterized by unsteadiness, boundary layer separation, shear layer instability and vortical flow motions with recirculation and reattachment. Due to these intricate flow properties, the cavity flow is usually prone to aero-acoustic resonance. With deep cavities, discrete and energetic tones occur, while in shallow cavities broadband noise arises with high-level amplitudes. The acoustic resonance is related to large fluctuations in pressure, which may consequently have adverse effects on the stability of aircraft and the avionics housed in the cavity. The unsteadiness of a cavity flow is due to self-sustaining oscillations, which

are regulated by factors such as the flight speed, the cavity geometry and the incoming boundary layer properties.

Cavity flows have been extensively studied over the past 50 years since the pioneering work of Roshko [1], as reviewed recently by Colonius [2]. According to Stallings and Forrest [3] and Wilcox [4], four types of mean flow have been observed for cavities under supersonic conditions, namely, closed cavity, open cavity, transitional-closed cavity and transitional-open cavity. These have been further illustrated by Tracy and Plentovich [5] and recently by Grace [6]. Apart from the incoming boundary layer (and thus the freestream conditions), the classification has been mainly remarked by the cavity length-to-depth ratio, L/D. It is known that the pressure oscillation with closed cavities (with relatively small L/D) may lead to broadband noise, but may cause adverse static pressure gradient and make the separating store experience large nose-up pitching moments. With open cavities, by contrast, a nearly uniform pressure distribution is produced along the cavity, which is desirable for safe store separation. However, high-intensity acoustic tones are developed at discrete frequencies [7], leading potentially to vibrations and consequently structural fatigue. Apparently, these phenomena are justifiable by studies of the flow characteristics which are closely coupled with the pressure oscillations. Moreover, the acoustic tones generated from an open cavity flow have been often understood being a consequence of the interaction between the shear layer that bridges the cavity and the cavity aft wall on which the shear layer impinges [8]. Corresponding to characteristic pressure patterns (standing waves and modes) in the cavity, these acoustic tones occur at discrete frequencies, which can be approximately determined by the semi-empirical Rossiter formula [9], viz.

$$f_n = \frac{U_\infty}{L}\frac{n-\gamma}{M_\infty + 1/\kappa}, \tag{1.1}$$

where U_∞ and M_∞ are the freestream velocity and Mach number, respectively, L is the length of the cavity, n is the mode number, γ and κ are two empirical constants.

Two typical modes in triggering the flow oscillations have been often discussed, namely, the *shear-layer mode* and the *wake mode*. The shear-layer mode exists for open cavities, where the shear layer, emanating from the cavity leading edge, impinges on the cavity aft wall and entails intensive flow fluctuations. When the cavity length-to-depth ratio increases, the shear-layer mode may shift to the wake mode due to the breakdown of the shear layer with vortex shedding. In either of the cases, the flow is often characterized by turbulence. Apart from a number of previous analytical and experimental studies, great effort has been made to investigate cavity flows using CFD technique incorporated with different turbulence models to deal with the turbulence effect, as reviewed by Grace [6]. Among others, Reynolds-Averaged Navier-Stokes (RANS) modelling approaches have long and commonly been used, see e.g. [10, 11, 12]. It has been shown that the modelling of turbulence may impose essential impact on the simulation of flow field and pressure fluctuations in the cavity. The key to the enhancement of computational accuracy is to model the turbulent shear layer and its instabilities. Turbulence affects significantly the instabilities of the shear layer and its mixing capabilities when travelling downstream. Consequently, the strength of the impingement of the shear layer on the cavity aft wall is influenced by the turbulence predicted in the shear layer. In simulations of turbulent cavity flows, turbulence modelling is thus one of the most important ingredients in order to achieve reliable flow predictions.

The work presented in this report is a continuation of a previous study, where a number of 2D URANS computations were performed for a subsonic

flow past a $5:1$ rectangular cavity at a freestream Mach number of $M_\infty = 0.85$ with a Reynolds number as high as $Ra = 7 \times 10^6$ [13]. The present work is dedicated to a three-dimensional simulation using unsteady RANS (URANS) modelling, of which the results will be further compared with a detached eddy simulation (DES) [14]. The cavity geometry mimics a weapon-bay configuration during a store-release operation (with a door-off configuration). The experiment was conducted by QinetiQ [15, 16], from which the measured time series of pressure fluctuations are available for a number of locations on the cavity wall surface. Comparisons have been made between the 3D URANS computation and the experimental measurement with an emphasis on the analysis of pressure fluctuations and the resulting sound resonance. Using the database from a well-resolved large eddy simulation (LES) by Larcheveque et al. [17], we have also made some observation on the mean flow field averaged over a long time period, as well as on the unsteady flow field by means of snapshots at arbitrary instants. In the following section, an introduction about the simulation methodology will be given first, including some numerical aspects and the turbulence model used. In Section 3, the results are presented and being accompanied with discussion. A summary and some concluding remarks are then given in Section 4.

2 Simulation Methodology

In this section, the numerical aspects used in the computation are briefly described. These include the CFD solver, EDGE, and some related numerical specifications.

2.1 The Navier-Stokes Solver

The simulation has been carried out using the FOI unstructured Navier-Stokes solver EDGE, which is a node-based Euler/Navier-Stokes solver for the compressible flow equation system using finite volume method [18]. Here, only a brief description is given on the schemes related to unsteady computations.

The equation system to be solved is written in a symbolic form of

$$\frac{\partial q}{\partial t} + \mathcal{C}(q) + \mathcal{D}(q) = S_q, \tag{2.1}$$

where the convection and viscous terms are expressed respectively by the operators $\mathcal{C}$ and $\mathcal{D}$, and S indicates the source term, see e.g. Hirsch [19] for details. The solution vector q in Eq. (2.1) contains the conservative variables, $q = (\rho, \rho u, \rho v, \rho w, \rho E, \rho\phi)^T$, for the density ($\rho$), three velocity components (u, v and w), the total energy (E) and the turbulence quantity (ϕ), respectively. Note that ϕ is used here to indicate one or more turbulence variables, upon the number of turbulence transport equations solved in the model. With the Spalart-Allmaras model [20], for example, ϕ represents the working turbulent eddy viscosity, $\tilde{\nu}_t$.

The EDGE solver is "grid-transparent" since it is equally applicable to any type of meshing element. An edge-based formulation and a preprocessor that translates element-based information to edge-based information allows the system to handle structured, unstructured and hybrid grids. A dual grid forms the control volumes with the unknowns in the centers. The governing equations given symbolically in Eq.(2.1), integrated over an arbitrary control volume, Ω, with a boundary, S, can be cast in a general form

$$\frac{\partial}{\partial t}\int_\Omega q d\Omega + \oint_S \left[F_c(q) - F_d(q)\right]\vec{n}\cdot d\vec{S} = \int_\Omega S(q) d\Omega \tag{2.2}$$

where $F_c(q)$ and $F_d(q)$ are respectively the convective and diffusive fluxes over the control volume faces, $\vec{n}$ is the normal vector outwards the face.

The convective flux is approximated with a second-order central scheme for the Navier-Stokes equations, and a second-order upwind scheme of the Roe's flux difference splitting type is employed for the turbulence transport equation. In conjunction with the central scheme, an explicit scalar artificial dissipation is added using combined second- and forth-order differences, corresponding to a blend of first and third differences for the fluxes [21]. By resembling the Martinelli eigenvalue scaling for structured grids, the formulation used in EDGE gives a dissipation proportional to local spectral radius in the direction with grid stretching and a value slightly larger than the local spectral radius in

the other directions [18]. When multigrid is used, on coarser grids a simplified form of the artificial dissipation operator based on the second difference is used.

The viscous flux is estimated by splitting the viscous operator in normal and tangential derivatives. The normal derivatives are approximated on the edges, by which only two points are involved in computing the normal gradients at the edges and thus leads to a compact second derivative. The remaining parts of the viscous terms contain gradients which may be added using a Green-Gauss formulation to obtain a fully viscous operator [18].

The time-dependent simulation is advanced using a dual-time stepping method [22], where a global physical time step, Δt, is employed and the local time step (the pseudo time step, $\Delta\tau$) is used in the subiterations based on an explicit three-stage Runge-Kutta scheme. At each physical time step, the computation is taken as for a steady-state calculation with the use of the maximum allowable time step locally without violating the numerical stability criterion. Due to the disparity in mesh sizes for viscous calculations, the local time step, $\Delta\tau$, is define by $\Delta\tau = \min(\Delta\tau_I, \Delta\tau_V)$, where $\Delta\tau_I$ and $\Delta\tau_V$ are the time steps set respectively by the inviscid and the viscous stability constrains. Given the governing equation, Eq. (2.2) is rewritten in terms of the time derivative and the residual, $\mathcal{R}(q)$, that includes the convective, diffusive fluxes and the source term, namely, $\mathcal{R}(q) = \{\mathcal{C}(q) + \mathcal{D}(q) - S_q\}$. With the introduction of a fictitious time, τ, the unsteady Navier-Stokes equation can be reformulated as

$$\frac{\partial q}{\partial \tau} = -\left[\frac{\partial q}{\partial t} + \mathcal{R}(q)\right] \tag{2.3}$$

With an efficient steady-state flow solver, the reformulated equation, Eq. (2.3), can be driven to a "steady state" at each physical time step. Consequently, the pseudo-time derivative becomes zero, and the original Navier-Stokes equations are recovered. In the present computation, the physical time derivative has been discretized with a three-point backward differencing formula, which is second-order accurate in time,

$$\frac{\partial q}{\partial \tau} = -\left[\frac{3q^{n+1} - 4q^n + q^{n-1}}{2\Delta t} + \mathcal{R}(q^{n+1})\right], \tag{2.4}$$

where the index $(n+1)$ denotes the present physical time step. At each time step, Δt, the numerical solution is iterated using a three-stage Runge-Kutta time marching algorithm, in which the numerical as well as the physical diffusion are computed at the first stage. Note that the time-discretization in Eq. (2.4) is fully implicit, which is A-stable. Nonetheless, stability problems may occur when the stepping in the pseudo time, τ, exceeds the physical time step. This happens in general in viscous computations due to the severe grid stretching to resolve near-wall boundary layers. The local time step has to be limited for unsteady computations by the physical time step, that is,

$$\Delta\tau = \min\left[\Delta\tau_0, CFL_\nu \frac{2\Delta t}{3}\right], \tag{2.5}$$

where $\Delta\tau_0$ is the local time step estimated for a steady computation of the problem, CFL_ν is the viscous CFL number which is an user-input parameter in EDGE (i.e. CFLVIS). Additionally, implicit residual smoothing is employed to effectively stabilize the convergence. The convergence is accelerated with agglomeration multigrid, for which the coarse grid corrections are smoothed using the same implicit residual smoother. A pre-processor has been used to agglomerate coarser control volumes for the multigrid and to split up the computational domain for parallel MPI calculations.

2.2 The Spalart-Allmaras RANS Model

The results presented here have been computed using the Spalart-Allmaras (S-A) turbulence model [20]. The S-A model solves the transport equation for a working eddy viscosity, $\tilde{\nu}_t$, which was constructed using empiricism and arguments of dimensional analysis, Galilean invariance, and selective dependence on the molecular viscosity [20]. In the empirical assemble of the turbulence transport equation, the model has undergone a series of calibrations in analysis of free shear flows, near-wall effects of wall-bounded flows, and for viscous flows past solid bodies with laminar-turbulence transition by means of tripping. Without including the function of transitional tripping, the S-A model for fully developed turbulent flows reads

$$\frac{D\tilde{\nu}_t}{Dt} = C_{b1}\tilde{S}\tilde{\nu}_t + \frac{1}{\sigma}\left\{\frac{\partial}{\partial x_j}\left[(\nu+\tilde{\nu}_t)\frac{\partial\tilde{\nu}_t}{\partial x_j}\right] + C_{b2}\frac{\partial\tilde{\nu}_t}{\partial x_j}\frac{\partial\tilde{\nu}_t}{\partial x_j}\right\} - C_{w1}f_w\left[\frac{\tilde{\nu}_t}{d}\right]^2 \quad (2.6)$$

with

$$\tilde{S} = S + \frac{\tilde{\nu}_t}{\kappa^2 d^2}f_{\nu 2} \text{ and } f_{\nu 2} = 1 - \frac{\chi}{1+\chi f_{\nu 1}} \quad (2.7)$$

where S is the magnitude of vorticity, d is the local wall distance. The turbulence eddy viscosity is computed by

$$\nu_t = f_{\nu 1}\tilde{\nu}_t, \quad f_{\nu 1} = \frac{\chi^3}{\chi^3 + c_{\nu 1}^3} \text{ and } \chi = \frac{\tilde{\nu}_t}{\nu} \quad (2.8)$$

Consequently, the turbulent stresses are computed by means of $-\rho\overline{u_i u_j} = 2\mu_t S_{ij}$, where S_{ij} is the flow strain rate tensor. The function f_w is designed to accommodate the "wall-blocking" effect in conjunction with the destruction term [20], which is empirically set as

$$f_w = g\left[\frac{1+c_{w3}^6}{g^6+c_{w3}^6}\right], \quad g = r + c_{w2}(r^6 - r) \text{ and } r = \frac{\tilde{\nu}_t}{\tilde{S}\kappa^2 d^2} \quad (2.9)$$

Note that both values of r and f_w are unique in the log layer and decrease in the outer region. The function of f_w thus disappears in free shear flows and $f_w < 1$ in the outer part of a boundary layer to justify the destruction term. The model constants are $c_{b1} = 0.1355$, $c_{b2} = 0.622$, $\sigma = 2/3$, $\kappa = 0.41$, $c_{w1} = c_{b1}/\kappa^2 + (1+c_{b2})/\sigma$, $c_{w2} = 0.3$, $c_{w2} = 2$, $c_{\nu 1} = 7.1$. For turbulent heat transfer, the turbulent Prandtl number is set by $Pr_t = 0.9$.

The S-A model has been chosen in the present computation, because this model has shown promising performance in aerodynamic flow simulations with separation in many previous computations. In addition, the model consists of only one turbulence transport equation to solve, which is more computationally efficient in time-dependent computations. Furthermore, this open-cavity flow has also been calculated using detached eddy simulation (DES) based on the S-A DES model. An intention is to make comparative studies of the results computed respectively from the S-A URANS and DES modelling approaches using the same mesh, which will be reported separately. This may help to shed a light on the merits and disadvantages of the two modelling methods, which have been attracting noticeable attention in studies of turbulence modelling and applied computational aerodynamics.

2.3 The Computational Set-up

The geometric configuration of the cavity used in the computation is the same as in the experiment conducted by QinetiQ [15, 16]. The three-dimensional

generic cavity rig was mounted in a $8' \times 8'$ transonic wind tunnel. The open cavity (termed *M219 cavity* hereafter) is contained in a flat plate with a length of 72 inches and 17 inches in width. The M219 test case includes two configurations for the cavity embedded in the flat plate. The two configurations differ only in that one was tested with bay doors open at 90 degrees and the other with bay doors removed. The former (i.e. *door-on*) is more two-dimensional in feature on the mid-section of the cavity due to the blocking of spanwise flow entrainment by the doors [23]. The measurement with this *door-on* configuration has thus been used in comparison with previous 2D computations as summarized in [13]. In the present three-dimensional computation, instead, the measurement with the *door-off* configuration is used for comparison. The rectangular empty cavity has dimensions of $L = 20$ inches in length, $D = 4$ inches in depth and $W = 4$ inches in width, giving a ratio of $L : D : W = 5 : 1 : 1$, see Figure 2.1. The experiment was performed under freestream conditions of $M_\infty = 0.85$, $P_\infty = 6.21 \times 10^4 Pa$, $T_\infty = 266.53K$ and $Re = 13.47 \times 10^6$ per meter.

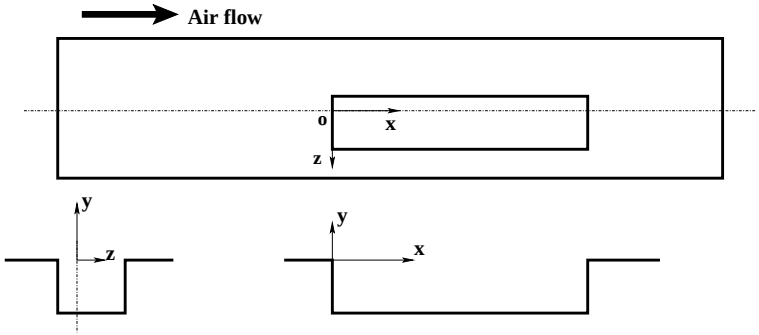

Figure 2.1: The experimental sketch of the cavity geometry embedded in a 72 inches $\times$17 inches flat plate for measurement.

The experimental data consist of time histories of pressure measured at various locations on the cavity floor and walls, and at locations on the plate wall surface upstream and downstream of the cavity. The time histories of wall-surface pressures were measured at a frequency of 6 kHz at a number of locations including 10 equally spaced points along the cavity floor.

The computational domain, shown in Figure 2.2, is specified with dimensions of $L_x \times L_y \times L_z = 18D \times 17D \times 9D$ in the $x-$ (streamwise), $y-$ (vertical) and $z-$ (spanwise)directions, respectively, where D is the depth of the cavity. The upstream distance from the leading edge of the flat plate to the front wall ($x = 0$) of the cavity is $7.75D$. The downstream distance from the cavity back wall ($x = 5D$) to the trailing edge of the plate is $5.25D$. Note that the origin of the coordinate system specified for the computational domain, Fig. 2.2, differs from that used in the experimental setup as illustrated in Figure 2.1. For the computational domain, the position of $z = 0$ has been located in the middle of the front wall of the cavity, which is embedded in the center of the spanwise z-direction. The extension of the flat plate, where the cavity is embedded, is larger in the spanwise direction (z-direction) with the computational domain than with the experimental setup. The distance is $4D$ from the cavity side wall to the spanwise boundary of the computational domain. This distance is observed to be enough to rule out the effect of the side edges of the plate on the flow in the cavity. The upstream and downstream extensions from the cavity are the same as in the experimental rig model. The upper boundary at $y = L_y$ is located at $L_y = 17D$ from the cavity opening, which is a distance

far enough to prevent any wave reflection from this boundary for any negative effect on the computational accuracy.

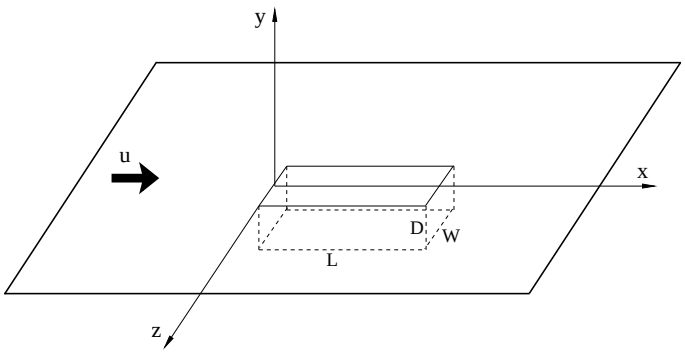

Figure 2.2: Sketch of the computational configuration. The cavity is embedded in a 72 inches $\times 36$ inches flat plate and is symmetric about the mid-section $z = 0$.

Location	Location	x (inches)	y (inches)	z (inches)
Front plate	k2	-4.0	0.0	-1.0
Front wall	k9	0.0	-1.0	1.5
Rear wall	*k17	20.0	-0.75	1.75
Floor	k20	1.0	-4.0	-1.0
	k21	3.0	-4.0	-1.0
	k22	5.0	-4.0	-1.0
	k23	7.0	-4.0	-1.0
	k24	9.0	-4.0	-1.0
	k25	11.0	-4.0	-1.0
	k26	13.0	-4.0	-1.0
	k27	15.0	-4.0	-1.0
	k28	17.0	-4.0	-1.0
	k29	19.0	-4.0	-1.0
	*k32	3.0	-4.0	0.5
	*k34	17.0	-4.0	0.5
Side wall	*k71	4.0	-1.0	-2.0
	*k72	8.0	-1.0	-2.0
	*k73	12.0	-1.0	-2.0
	*k74	16.0	-1.0	-2.0
Opening	*kmd	10.0	0.0	0.0

Table 2.1: Locations where pressure has been recorded in the computation. The computational coordinate system is the same as shown in Fig.2.2. Notation * indicates locations with no measured data available for the "door-off" case, but with experimental data for the "door-on" case. Location kmd is not experimentally measured in either of the cases, which is located in the center of the cavity opening.

For comparison with the experimental measurement, the pressure histories have been recorded in the computation at 20 locations, as listed in Table 2.1. It should be noted that the location for these recorded points should be referred to the computational coordinate system shown in Figure 2.2, from which the experimental coordinate system is shifted 1 inch in the positive z-direction. In the "door-off" configuration, which is used for comparison with the present computation, the measured pressure histories are available at locations k2,

k9 and all the points along the cavity floor (k20-k29). At other locations, except for kmd, the pressure history has only been measured for the "door-on" configuration. In previous 2D computations, it was noticed that large magnitudes of pressure fluctuations may be entailed on the rear wall of the cavity, which may potentially induce structural damage. In the present 3D computation, the pressure histories have thus been recorded at one rear-wall location k17, as well as at locations k71-k74 on the cavity side wall. The location kmd has been chosen in order to observe the time-dependent flow property in the shear layer.

The cavity flow exhibits extensive pressure waves, it is thus important to ensure that the boundary conditions will not yield reflected waves that could affect the computational accuracy. As illustrated above, the far-field boundaries of the computational domain have been placed far enough away from the cavity. In addition, characteristic-based boundary conditions have been imposed on the inflow and outflow sections, as well as on the top boundary (i.e. at $y = L_y$). A symmetric boundary condition is assumed on the spanwise boundaries (at $z = \pm L_z/2$). Over all the wall surfaces, no-slip adiabatic wall boundary conditions have been imposed. For the turbulence quantity, $\tilde{\nu}_t = 0$ on the wall boundaries, and the freestream value was set as $\tilde{\nu}_{t\infty} = \nu/10$. A value of 1% was specified for the turbulence intensity in the incoming freestream.

In a previous 2D study [13] on the cavity flow, effort was made to investigate the effect of the mesh resolution. It was revealed that the grid resolution in the shear layer over the cavity opening and within the cavity is substantially significant to capture appropriately the amplitude and frequency of the first two Rossiter modes of the cavity pressure pattern. Prior to the present computation, several 3D meshes were tentatively tested, which were obtained on the basis of the 2D fine mesh by an extension of the domain in the spanwise direction with a refined grid between the two cavity side walls. Due to resolution near the walls with a structured grid, in this case, the flow region away from the wall layer was refined unnecessarily. Moreover, the grid stretching in the wall layer and over the cavity opening may induce a somewhat stiff numerical procedure in terms of the time step and other numerical settings for an unsteady simulation. In the present 3D computation, instead, a new mesh was used, which is boundary-fitted on the wall surfaces. An overall view of the mesh is illustrated in Figure 2.3, showing that a O-type mesh around the cavity opening is gridded over the plat surface.

In Figure 2.4, the grid in some interesting regions has been zoomed to have

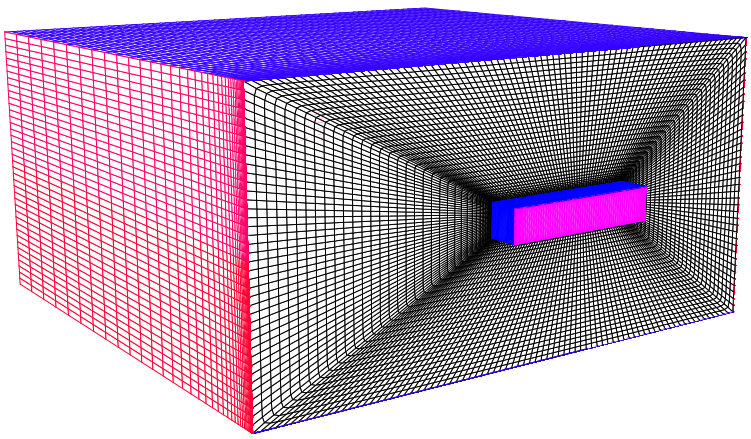

Figure 2.3: An overall view of the computational mesh.

a detailed insight on the local meshing. It is noted that the mesh has been made for mapping the wall layer along all the wall surface. This has helped to save some unnecessary grid nodes. In order to diminish inaccuracy in computations of the convective and diffusive fluxes, the mesh in the vicinity of a wall surface has been gridded with orthogonal cells, as shown in Figure 2.4 (c) and (d). The mesh contains about 1.26 million nodes, of which about 180000 nodes have been placed within the cavity. The first node close to the wall has a wall distance less than 4×10^{-6} m in general. It should be noted here that the number of grid nodes contained in a 2D *xoy*-plane cut within the cavity is actually less than that in the previous 2D RANS calculation with the coarse mesh [13].

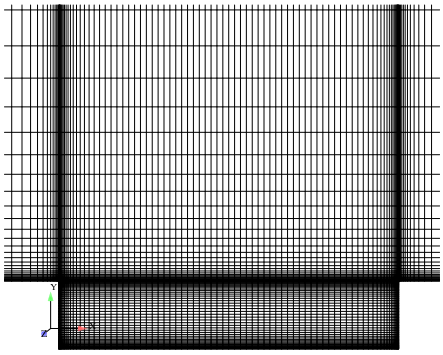

(a) Meshing on section $z = 0$.

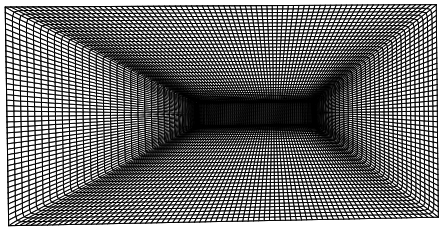

(b) Meshing on plane $y = 0$.

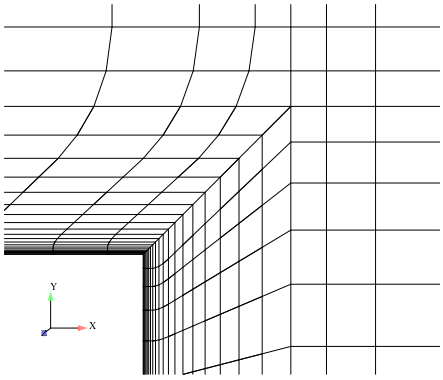

(c) Meshing around the front-edge upper corner of the cavity.

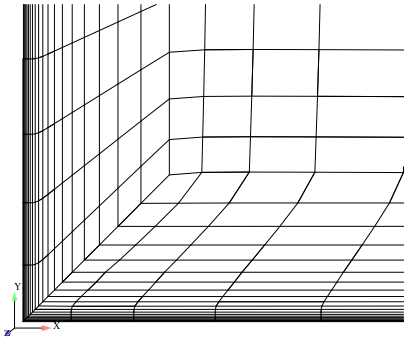

(d) Meshing around the down corner of the cavity.

Figure 2.4: Illustration of the meshing around the cavity walls.

The initial flow field was obtained by running a steady RANS computation with the S-A model. The time step used in the unsteady calculation is $\Delta t = 5 \times 10^{-6}$ second, which is smaller than those used in computations by, for example, Ashworth [23] and by Larcheveque et al. [17]. The reason that we have employed such a small time step is due to the consideration of maintaining a better numerical stability and of reducing the number of sub-iterations at each time step. Nevertheless, our late unsteady computations have demonstrated that this time step can be increased up to $\Delta t = 2 \times 10^{-5}$ without deteriorating the computational accuracy by only marginally increasing the sub-iteration number at each time step. The unsteady RANS computation started on the previous FOI compact computer system with an earlier EDGE version, which at that time was not so efficient for unsteady computations. After running several thousands of time steps, the FOI computing facility has been upgraded to the a new cluster machine and the EDGE solver has also been updated. Instead of

re-doing the computation using a larger time step, the calculation was carried on with the same numerical settings. On the old compact machine, 8 CPUs were used, and it took about 35 CPU seconds to perform one sub-iteration. With the new FOI cluster, 24 CPUs were allocated in the computation, and about 7-10 CPU seconds were required for each sub-iteration. It is noted here that a larger time step has been adopted in a separate DES computation with the same mesh. In a study about the effect of temporal resolution, Larcheveque et al. [17] performed LES using different time steps for the same cavity flow, which illustrated that the time steps with $\Delta t = 2 \times 10^{-5} s$ and $\Delta t = 10^{-5} s$, respectively, gave very similar results. In the DES computation [14], a time step of $\Delta t = 10^{-5} s$ has been employed, which entails an effective numerical procedure with the new EDGE version. In the following section, the URANS results are presented and discussed.

3 Results and Discussion

The simulation consists of two parts of results. The first part includes the time histories of the surface pressures, $P(t)$, at locations as listed in Table 2.1, which were recorded at each time step. In addition, a series of unsteady flow fields have been saved. Another part of the solution includes the mean flow field obtained by means of time-averaging over a sufficiently long time period. The computation has been carried out for about 23000 time steps, of which the first 2000 time steps have been discarded in the analysis of the pressure time series and for the time-averaging to obtain the mean flow properties.

The pressure oscillation is closely related to the sound resonance from the cavity. As done in 2D analysis [13], the recorded $P(t)$ has been used to compute the power spectral density (PSD) and the sound pressure level (SPL) as functions of frequency, f. The discrete Fourier transform has been used for $P(t)$ to compute the PSD. The sound pressure level (SPL) is then obtained from the calculated PSD, which is defined by

$$SPL = 20 \log \left(\frac{\sqrt{PSD}}{p_{ref}} \right), \tag{3.1}$$

where $p_{ref} = 2 \times 10^{-5}$ Pa is the value adopted as the minimum audible sound pressure variation.

In addition, the mean pressure, $\overline{P}$, and the root mean square, r.m.s, of the pressure, P_{rms}, have been calculated, respectively. The time-averaged sound pressure level or the pressure intensity, $\overline{SPL}$, has been estimated consequently from

$$\overline{SPL} = 20 \log \left(\frac{P_{rms}}{p_{ref}} \right). \tag{3.2}$$

For the "door-off" configuration, the experiment measured the time series of fluctuating surface pressure, but the experimental data for PSD was not available. For comparison with the computation, the same discrete Fourier transform is applied to the measured $P(t)$ data in order to obtain the *measured* PSD and SPL from the experiment. For comparison of the mean flow field, the data from the full LES by Larcheveque et al. [17] is used. The LES used the selective mixed-scale model for computing the subgrid-scale eddy viscosity. Two meshes were employed for grid convergence studies. The coarse mesh contains about 3 million cells, of which one million nodes were gridded in the cavity. The fine mesh was double refined over the coarse mesh. Some discrepancies were observed between the results obtained from the two LES meshes. The present URANS results have been compared with the LES data computed from the fine mesh.

3.1 Sound Resonance Due to Pressure Oscillations

With a length-to-depth ratio of $L/D = 5$ and at a freestream Mach number of $M_\infty = 0.85$, the flow shows some features of open-cavity type, for which

the shear layer may bridge over the cavity opening. Due to the self-sustaining oscillations, high-intensity acoustic tones may be generated. The experimental observation indicates the existence of four Rossiter modes corresponding to the characteristic pressure patterns (standing waves or modes). These modes have experimentally identified frequencies of, respectively, $f_1 = 135Hz$, $f_2 = 350Hz$, $f_3 = 590Hz$ and $f_4 = 820Hz$.

3.1.1 Pressure Fluctuations

In this section, the time series of the computed surface pressure fluctuations is presented in comparison with experimental measurements. Note that in the figures the time has been normalized by $T_0 = L/U_{ref}$. The running has advanced with about $65T_0$ in time, from which a time period of $20T_0$ is taken to illustrate the pressure fluctuations. In Figure 3.1, the pressure fluctuations recorded on the cavity floor (locations k20-k29) are compared with measured data. Note that the measured pressure fluctuations have been arbitrarily taken (but with a time period of $20T_0$) from the experimental data set. Surprisingly, the URANS simulation produces very *rich* fluctuations for the surface pressures, which are even comparable with the DES computation [14]. According to the Rossiter formula [9], there are two phenomena characterizing the feedback loop: the mixing layer vortices moving downstream at a velocity of κU_∞ and the pressure waves travelling upstream inside the cavity at the speed of sound. This has actually been reflected in Eq. (1.1). The predicted fluctuating intensity of the surface pressure in the cavity is thus closely related to the prediction of the mixing layer impinging on the cavity aft wall and of the resulting flow motion in the cavity. The 3D URANS simulation has reproduced significantly improved surface pressures than previous 2D URANS as presented in [13]. This is particularly the case for points located in the front part on the floor ($x/L < 0.5$). In the rear part on the floor (i.e. for $x/L > 0.5$), nonetheless, the peaks of the fluctuations are sensibly over-estimated. This has led to an over-prediction of the r.m.s of pressure fluctuations on the cavity floor, as shown in Figure 3.2. The general tendency for P_{rms} has been well reproduced, however, with an increasing pressure fluctuation along the cavity floor. After $x/L \geq 0.5$, the discrepancy between the computation and the measurement becomes increasingly large. The over-estimation in P_{rms} on the floor near the rear wall is an indication that the strength of the shear layer may have been under-estimated so that a part of the fluid in the mixing layer has been deflected to the cavity floor, prior to the impingement to the cavity aft wall. It has caused intensified field fluctuations when this part of fluid approaches the cavity floor. This will be further addressed in the observation of the flow field.

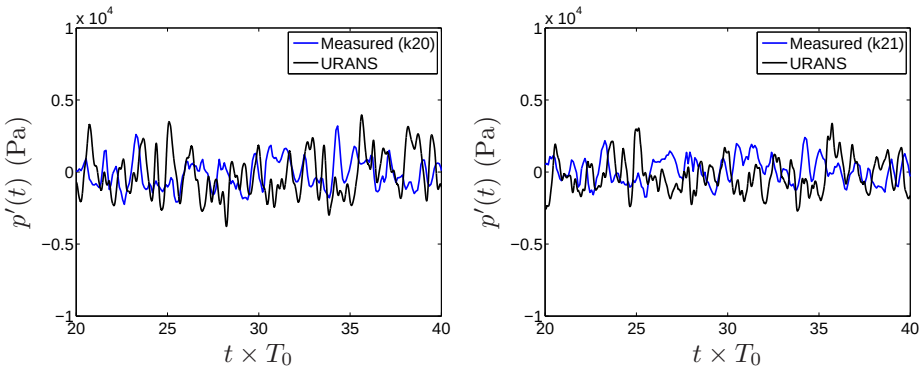

(a) Position k20. (b) Position k21.

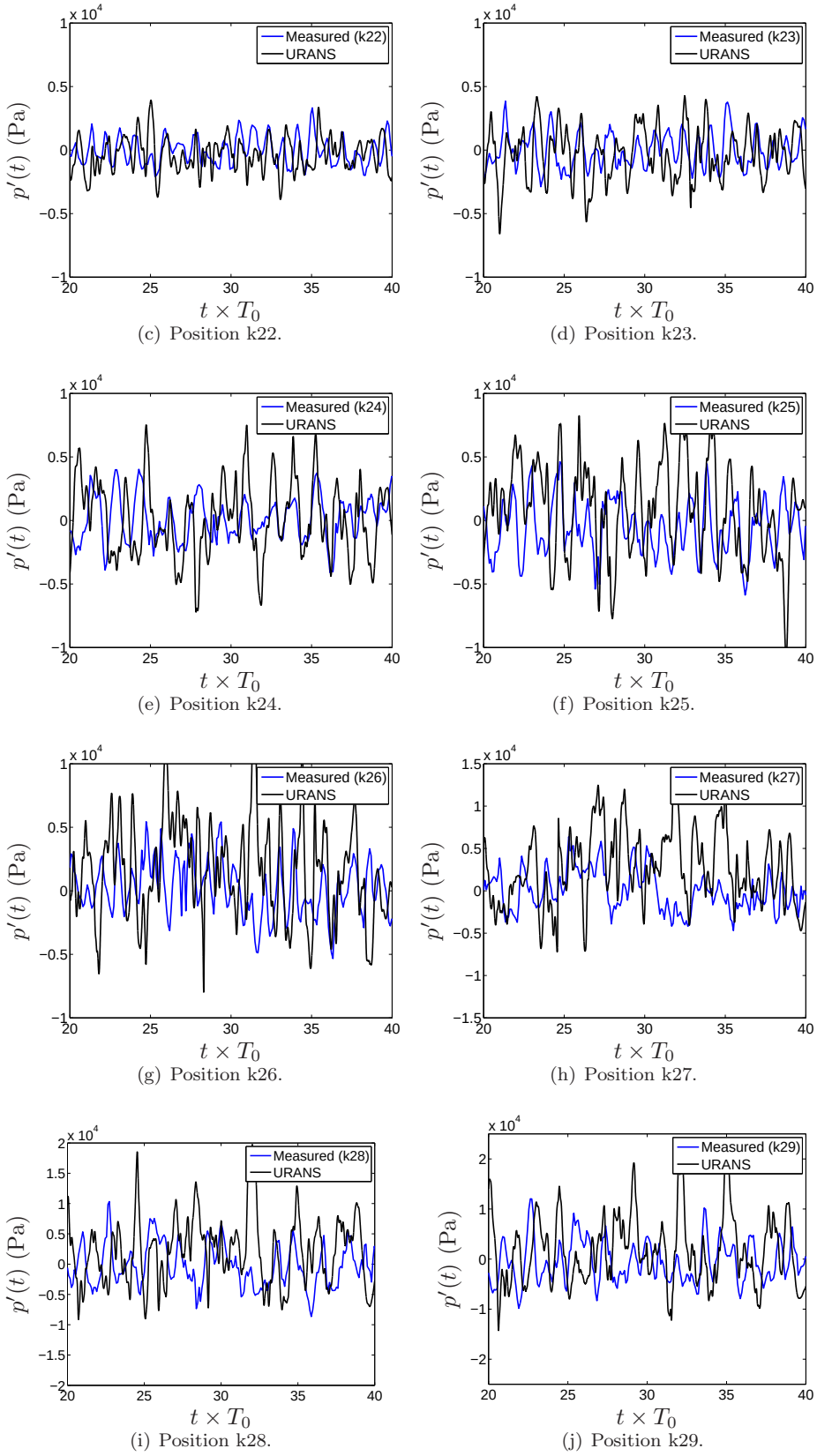

(c) Position k22. (d) Position k23.

(e) Position k24. (f) Position k25.

(g) Position k26. (h) Position k27.

(i) Position k28. (j) Position k29.

Figure 3.1: Pressure fluctuations on the cavity floor at locations k20, k21, k22, k23, k24, k25, k26, k27, k28 and k29.

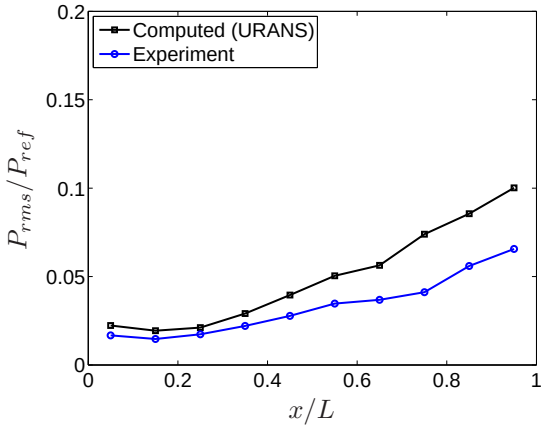

Figure 3.2: Computed root mean square of surface pressure fluctuations, P_{rms}, along the cavity floor in comparison with the experimental measurement.

Figure 3.3 summarizes the time series of $P(t)$ at other locations. Note that the experimental measurement was only conducted at locations k2 and k9. Also, point *kmd* is located in the mixing layer in the center of the cavity opening. Position k2 is placed on the wall surface below the upstream incoming boundary layer prior to the cavity leading edge, where both the experiment and the computation indicate low-amplitude pressure fluctuations but the experimental measurement exhibits more intensive high-frequency fluctuations. The pressure fluctuation at the cavity front wall (k9) has been reproduced very well, as compared with the measured data. At the cavity real wall (k17), the surface has undergone the most intensive pressure variation with the largest fluctuating amplitude. The relatively extensive fluctuation at k17 suggests that a part of the mixing layer has reached the cavity rear wall and impinging on it. The rear cavity wall takes a relatively large risk of structure fatigue due to large instantaneous surface pressures arising at relatively high frequencies. The pressure fluctuation in the mixing layer, kmd, is also rather extensive, of which the amplitude is comparable with those measured on the cavity floor surface. The same is for the level of $p'(t)$ taken on the side wall (k71-k74). Points k32 and k34 are located on the cavity floor, which are distant from the cavity leading edge with the same streamwise distance as points k21 and k28, respectively, but are closer to the mid-section ($z = 0$). The fluctuation amplitudes at k32 and k34 are similar to k21 and k28, respectively. The pressure pattern over the spanwise direction seems to be fairly uniform on the cavity floor surface.

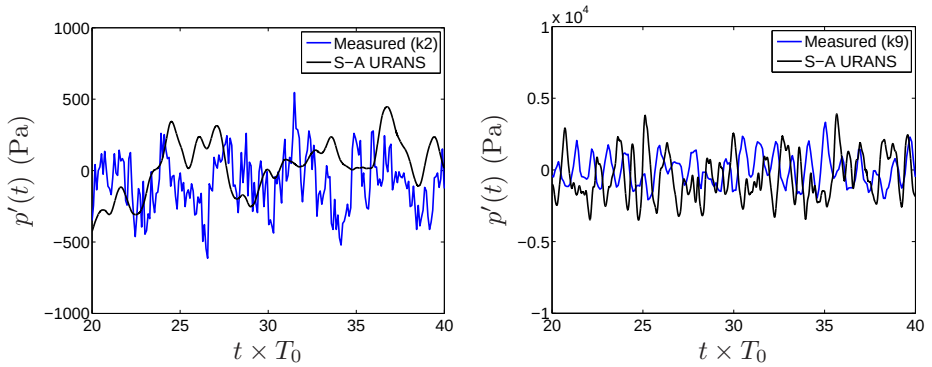

(a) Position k2. (b) Position k9.

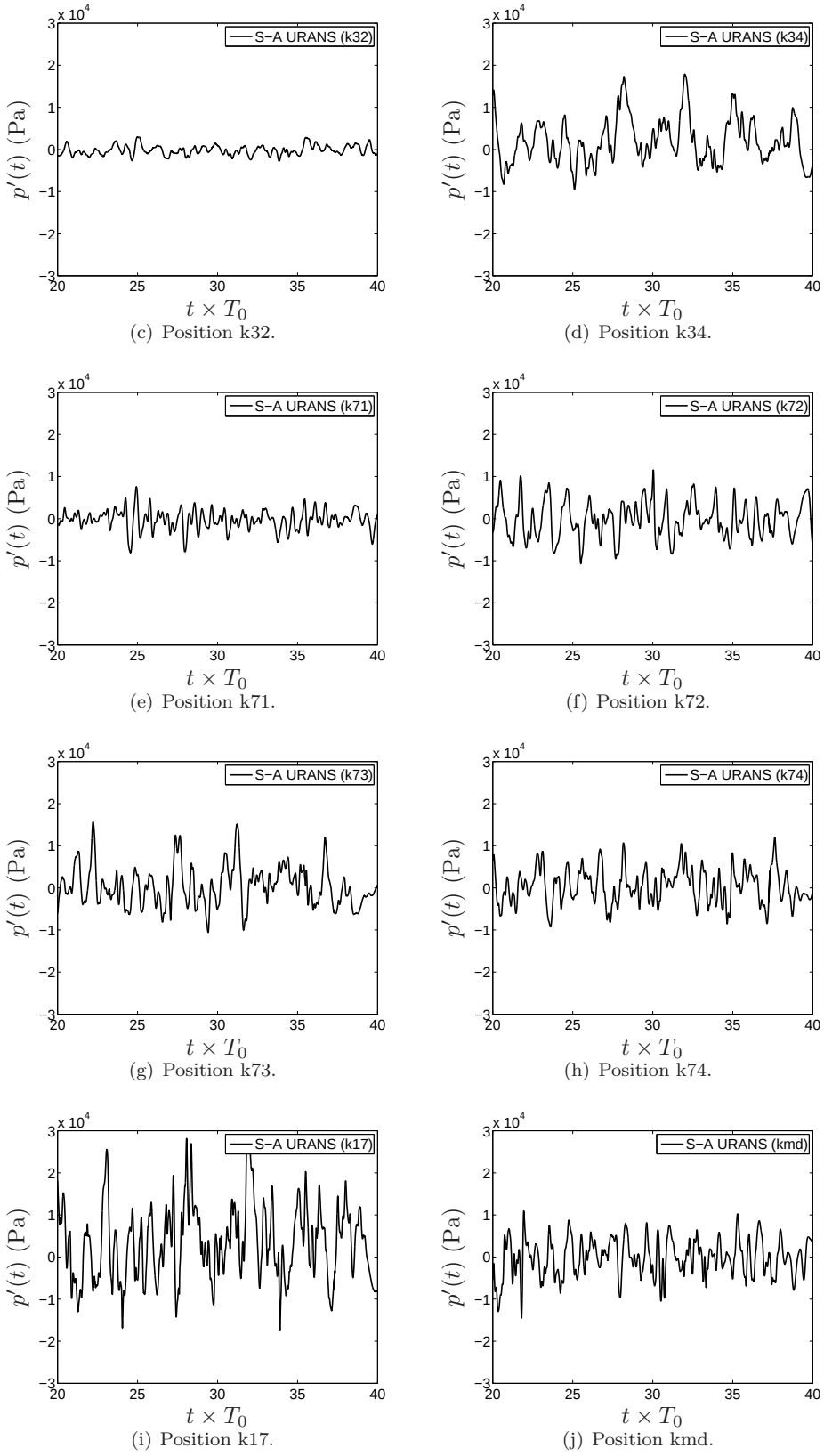

(c) Position k32. (d) Position k34.

(e) Position k71. (f) Position k72.

(g) Position k73. (h) Position k74.

(i) Position k17. (j) Position kmd.

Figure 3.3: Pressure fluctuations on the upstream plate (k2), cavity front wall (k9), cavity floor (k32, k34), cavity side wall (k71-k74), cavity rear wall (k17) and at the center of the cavity opening (kmd).

3.1.2 Analysis of Pressure Signal

In this section, an analysis is carried out for the sound resonance due to pressure oscillations in the cavity. It is known that, when the length of the cavity is long enough compared to the thickness of the incoming boundary layer, the pressure oscillation may generate acoustic tones at discrete frequencies [7]. The frequencies of these acoustic tones correspond to characteristic pressure patterns (standing waves or modes) in the cavity. The tones may trigger structural vibrations and lead to possible structural fatigue. To identify the tonal modes, the time series of fluctuating pressures is analyzed by means of the discrete Fourier transform, which gives PSD or SPL as a function of frequency, f. The experimental data for instantaneous pressure fluctuations have also been transformed using the same method.

The experimental observation has identified four main pressure modes (at frequencies of $f_1 = 135$ Hz, $f_2 = 350$ Hz, $f_3 = 590$ Hz and $f_4 = 820$ Hz, respectively), with the second and the third modes being the dominant ones. Figures 3.4 and 3.5 present the predicted PSD and SPL at positions along the cavity floor, respectively. As compared with those obtained from 2D computations [13], the agreement between the predicted and measured amplitudes of PSD (and thus SPL) have been obviously improved. Note that the peak in the spectra represents an acoustic tone (a pressure mode) at a corresponding frequency. The first mode at $f_1 = 135$ Hz is relatively weak, for which the simulation has produced a generally larger frequency with a less sensible spectral peak, as compared with the experimental data. In previous 2D computations, the 2D flow exhibited a periodic feature, and the frequency of the first mode corresponds to the time period of one flow cycle [13]. In the present 3D simulation, the flow does not exhibit obvious periodic features, as shown by the computed time series of surface pressures presented in Section 3.1.1. The predicted amplitudes of the second and third modes are generally comparable with the measured ones. The frequency f_2 for the second mode is however over-estimated. The third mode is better resolved in the front part than in the rear part of the cavity, which is somewhat smeared out at locations k26, k27 and k28. The flow near the cavity rear wall is subjected to a direct effect of the impingement of the mixing layer on the cavity aft wall, undergoing strong flow deformation. Apart from the turbulence modelling, grid refinement in this region is necessary to improve the accuracy of simulations.

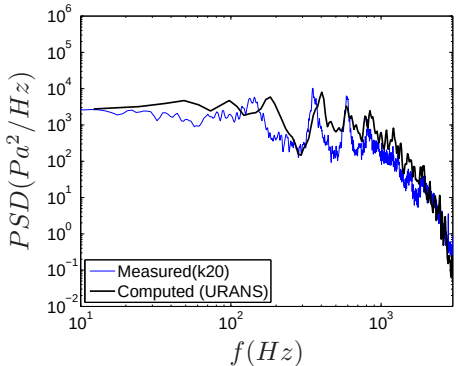

(a) Position k20.

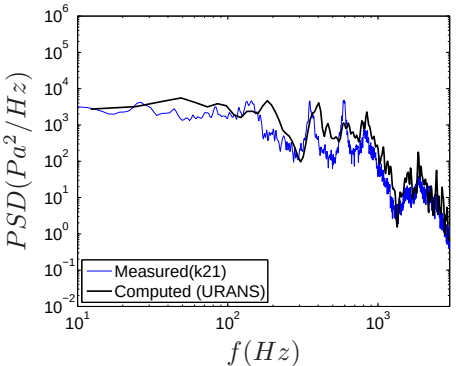

(b) Position k21.

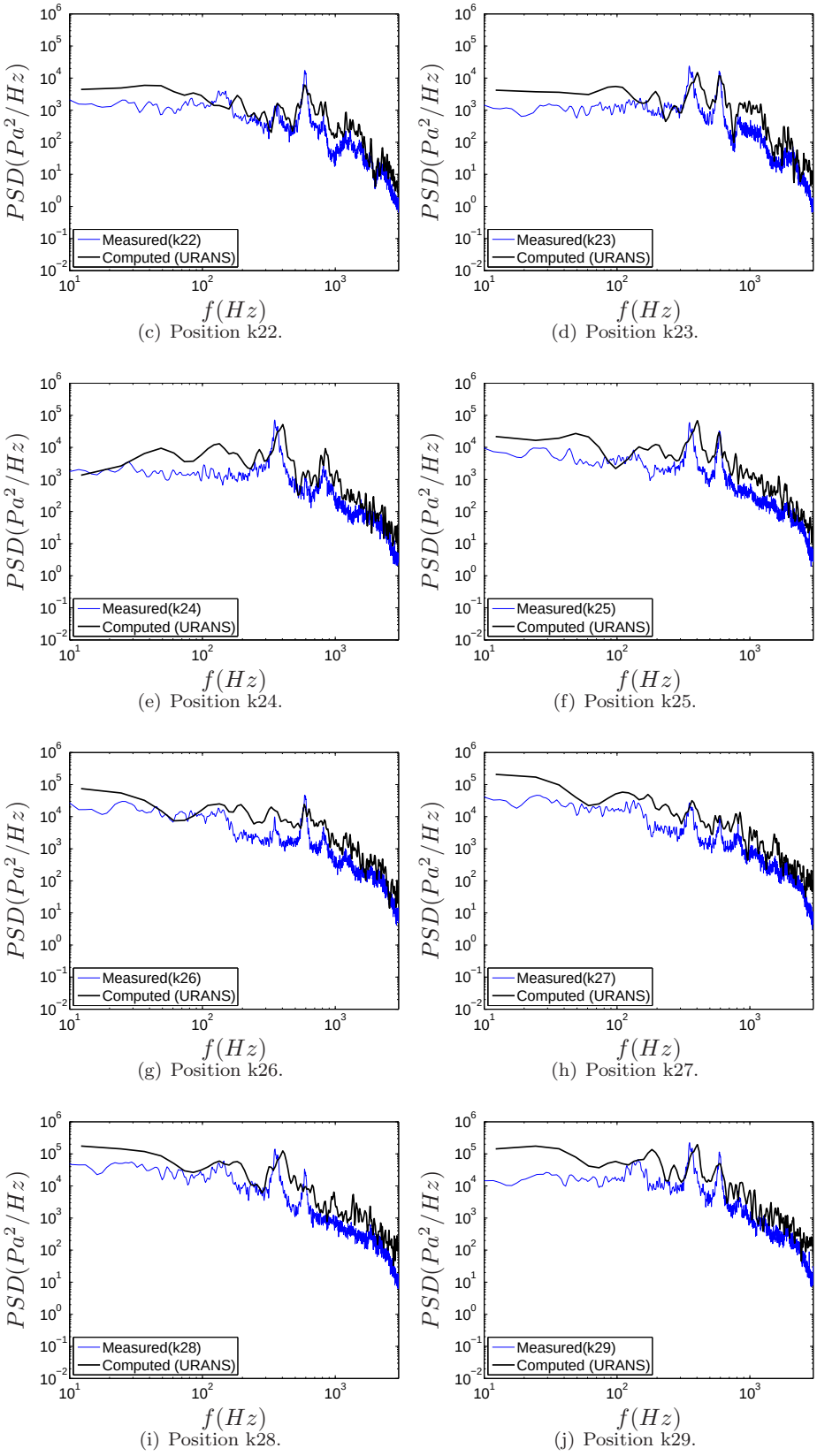

(c) Position k22. (d) Position k23.

(e) Position k24. (f) Position k25.

(g) Position k26. (h) Position k27.

(i) Position k28. (j) Position k29.

Figure 3.4: Computed PSD of pressure fluctuations at positions k20, k21, k22, k23, k24, k25, k26, k27, k28 and k29 on the surface of cavity floor.

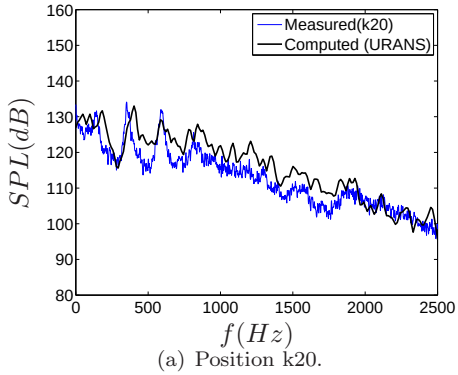

(a) Position k20.

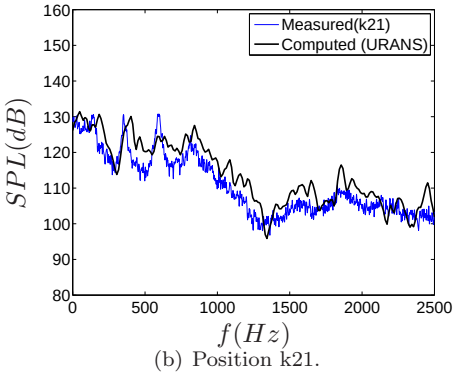

(b) Position k21.

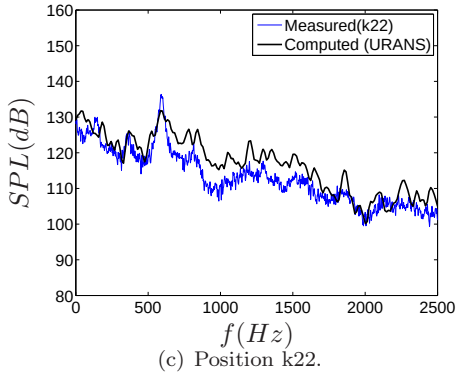

(c) Position k22.

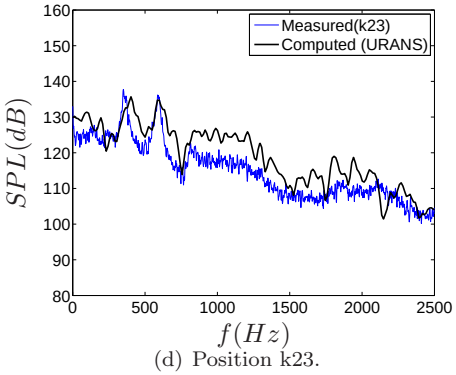

(d) Position k23.

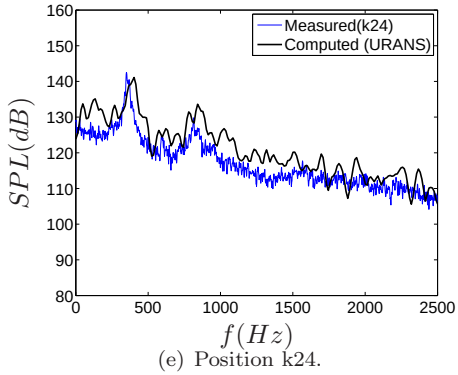

(e) Position k24.

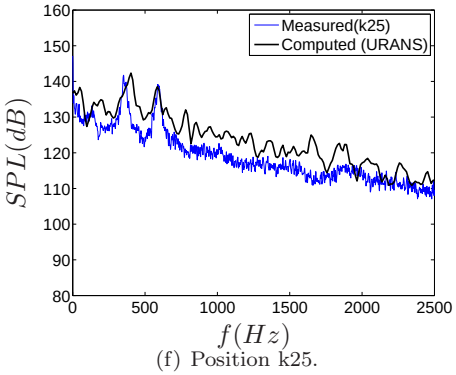

(f) Position k25.

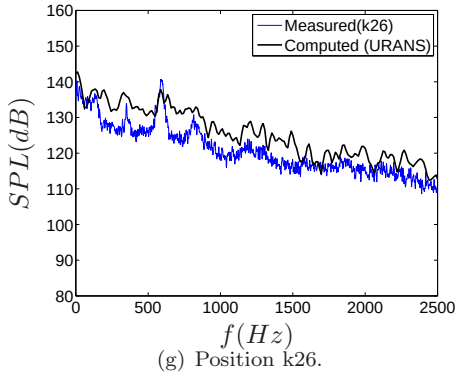

(g) Position k26.

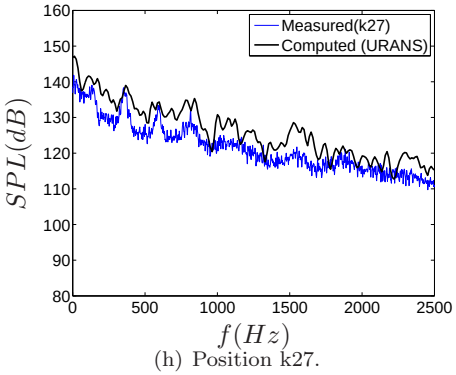

(h) Position k27.

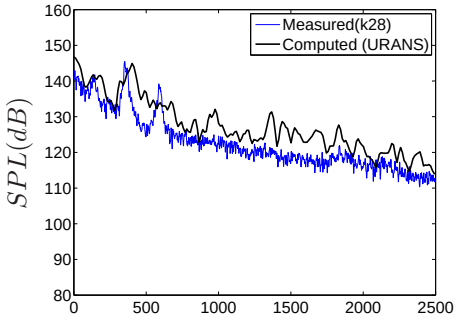

(i) Position k28.

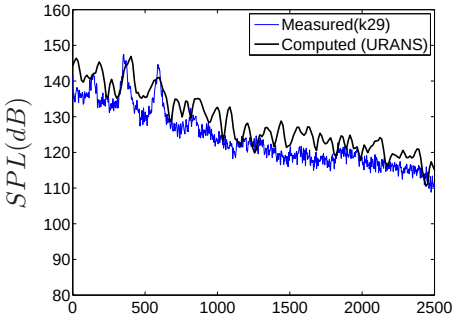

(j) Position k29.

Figure 3.5: Computed SPL at positions k20, k21, k22, k23, k24, k25, k26, k27, k28 and k29 on the surface of cavity floor.

In Figure 3.6, the predicted PSD and SPL are plotted for k9 and k17 located respectively on the cavity front and rear walls. There is no experimental data available for location k17, where the amplitude of PSD is generally larger than at other locations corresponding to the large pressure fluctuation. The predicted pressure modes are distinguishable at k9, but the frequencies to the first and second modes are somewhat over-estimated, and the amplitude of the third mode at k9 is under-predicted. On the rear wall (k17), the spectral peak for the third mode is somewhat smeared out. As mentioned, prior to the impingement on the aft cavity wall, a part of the fluid has been deflected from the mixing layer turning towards the cavity floor. Such a flow feature may have affected the prediction of the third mode at locations in the downstream rear part of the cavity (at k26-k28 and k17).

Figure 3.7 presents the PSD at locations on the side wall (k71-k74) and on the cavity floor (k32 and k34), where the experimental data are not available. At the side-wall locations, the spectral peak is not so verifiable as on the cavity floor, but the effect of the pressure modes persists. Note that location k32 and k34 are paired respectively with k21 and k28 for the same distances from the cavity front wall. The pressure modes are better captured at k32 than at k34, similar to the observation at locations k21 and k28 (see Figures 3.4 and 3.5).

Based on the computed PSD and SPL, the predicted frequencies for the four pressure modes have been identified. It should be emphasized here that URANS modelling seems to give fairly poor resolution at some locations for the first and forth pressure modes, which exhibit relatively small peak amplitudes. The estimated frequencies have been taken only at locations where the predicted pressure mode is distinguishable. Nonetheless, each mode has exhibited a consistent frequency at different locations, provided that the spectral peak is verifiable at the location. In Table 3.1 the frequencies for the four pressure modes are compared with the experiment and with the LES results by Larcheveque et al. [17]. Also included in the table is the frequencies estimated with the Rossiter formulation using $\gamma = 0.29$ and $\kappa = 0.57$ in Eq. (1.1) as done by Larcheveque et al. [17].

In Figure 3.8 (a), a comparison is made for the time-averaged sound pressure level, $\overline{SPL}$, see Eq. (3.2), at locations k20-k29 on the cavity floor, which is actually transferred from Figure 3.2 but is straightforward in relation to the sound resonance. It is shown that the URANS modelling has over-predicted $\overline{SPL}$. Note that $\overline{SPL}$ represents the pressure fluctuating intensity. As observed in the experiment, the computation has reproduced increasing pressure fluctuations along the cavity floor from the front wall to the rear wall. In Fig-

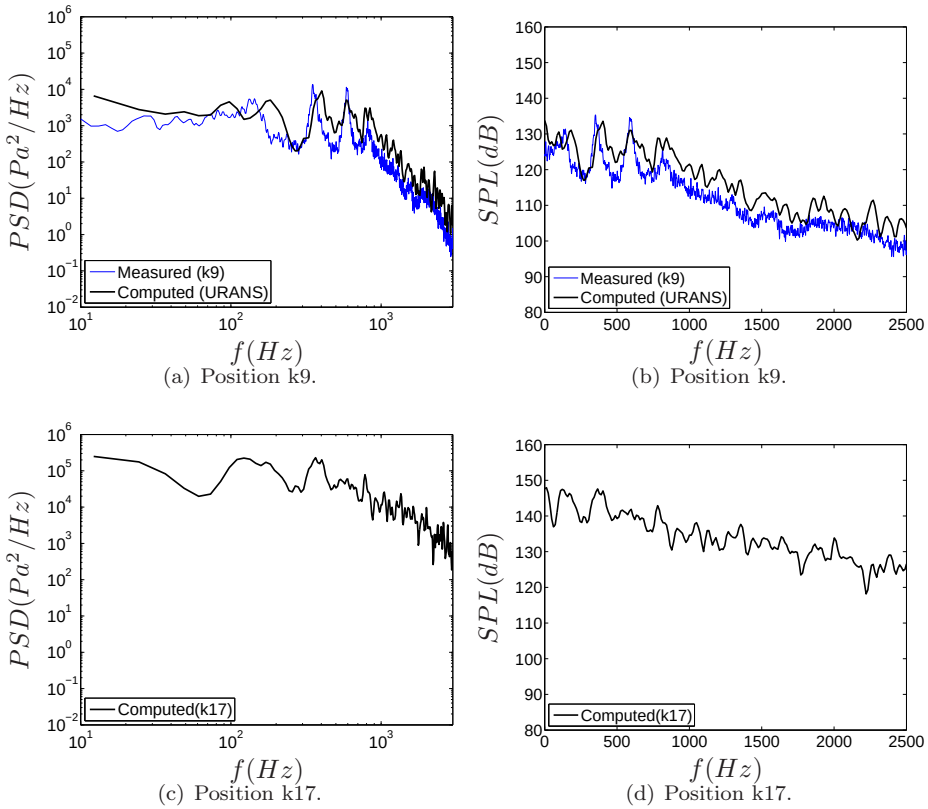

(a) Position k9. (b) Position k9. (c) Position k17. (d) Position k17.

Figure 3.6: PSD and SPL computed at the cavity front wall (k9) and rear wall (k17).

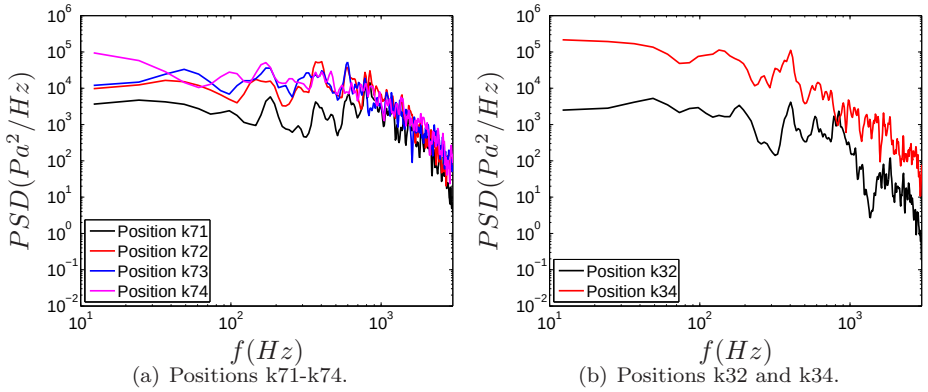

(a) Positions k71-k74. (b) Positions k32 and k34.

Figure 3.7: PSD computed on the side wall (k71-k74) and at locations k32 and k34 on the cavity floor.

Mode	1	2	3	4
Rossiter's formula	148	357	566	775
Experiment	135	350	590	820
LES (fine mesh)	125	355	575	815
URANS	176	400	586	842

Table 3.1: Frequency (Hz) of tonal modes due to pressure waves in the cavity.

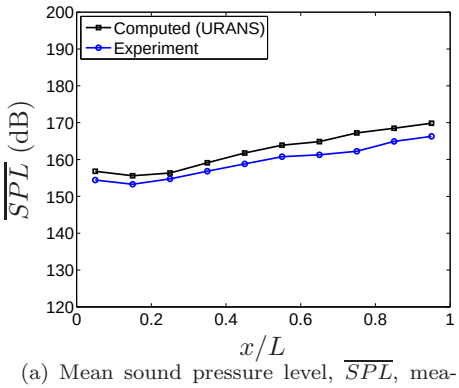

(a) Mean sound pressure level, $\overline{SPL}$, measured at locations k20-k29.

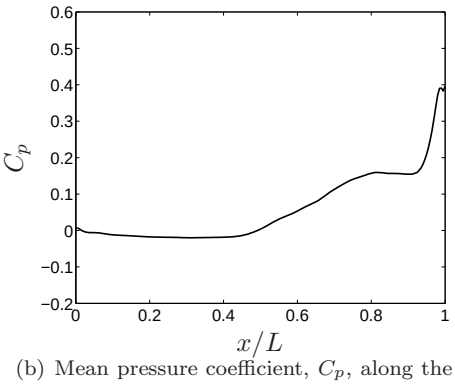

(b) Mean pressure coefficient, C_p, along the centerline of the cavity floor.

Figure 3.8: The computed mean sound pressure level, $\overline{SPL}$, and the mean pressure coefficient, C_p, along the cavity floor.

ure 3.8 (b), the mean pressure coefficient, $C_p = 2P/(\rho U_\infty^2)$, is plotted along the centerline of the cavity floor surface. As seen, the pressure distribution is fairly flat for $x/L \leq 0.5$ and then increases towards the aft cavity wall. Near the rear wall, the pressure presents a sharp increase with a large longitudinal pressure gradient. Such a pressure distribution is very similar to the type of transitional-open cavity flow, as described by Tracy and Plentovich [5]. The mean pressure has been further illustrated on the wall surface in Figure 3.9, which shows that high pressures exist on the rear wall, particularly around the corners. The high pressure level plus extensive fluctuations may potentially cause structure fatigue. Moreover, for store separation from the cavity, a uniform pressure distribution as for open cavity flows is usually preferred in practice.

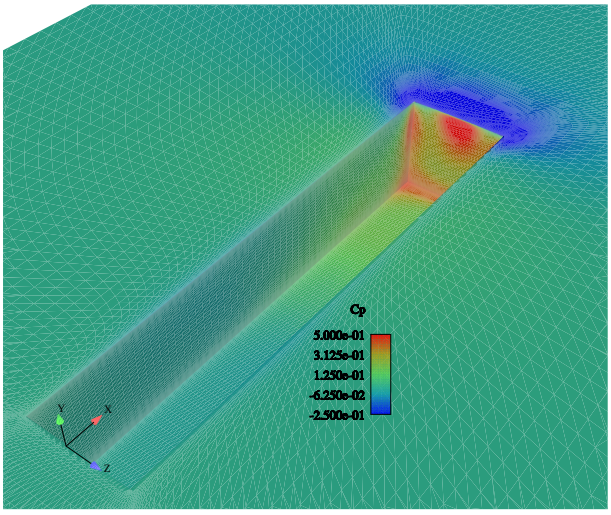

Figure 3.9: Mean pressure coefficient on the cavity wall surface.

3.2 Flow Field

The present cavity flow is to a large extent characterized by the *shear-layer mode* [8], for which the mixing layer bridges the cavity opening. The pressure

oscillation is of *fluid-resonant* type according to Rockwell and Naudascher [24], which is generated owing to the coupling between the shear layer and the pressure field. The self-sustaining process is closely related to the wave reflection within the cavity due to the impingement on the aft wall, and to the addition and removal of mass at the cavity trailing edge [24] in the case of a shallow cavity with sufficiently large length-to-depth ratio L/D. In previous 2D URANS computations, it was observed that the predicted unsteady flow exhibits an organized, periodical feature, and the periodicity of one cycle corresponds to the computed frequency of the first mode [13]. Nonetheless, in the above analysis of pressure fluctuations and of the consequent sound resonance, it has been implied that the strength of the mixing layer may have been under-estimated with a part of the fluids deflected from this layer and bended towards the cavity floor, prior to the impingement on the aft cavity wall.

In order to observe the property of the 3D unsteady flow field, Figure 3.10 illustrates the computed flow fields at a number of subsequent time instants, covering a time period of $4.6T_0$ with $T_0 = L/U_\infty$. In each illustration, the upper window presents the flow field on the zoy-plane at $x = L/2$ and the lower one gives the flow field on the xoy-plane at $z = 0$ (i.e. the mid-sections of the cavity in the streamwise and spanwise directions, respectively.) The velocity field has been colored by the turbulent eddy viscosity, which indicates the local turbulent intensity. The experiment gives a frequency of $f_1 = 135$ Hz for the first tonal mode in the pressure spectra, see Table 3.1. This corresponds to a periodicity of about $4.06T_0$. Figure 3.10, plotted over a time period of about $4.6T_0$, has clearly reproduced the time-dependent flow property. Unlike with 2D simulations, however, the present 3D simulation does not render any obvious periodical flow feature. Figure 3.10 shows that the flow is characterized by the shear layer over the cavity opening and by the recirculating motion within the cavity. The shear layer, emanating from the upstream boundary layer coming off from the cavity leading edge, spans the mouth of the cavity and stagnates at the rear wall. In spite of a relatively high freestream Mach number ($M_\infty = 0.85$), the flow is of essentially subsonic type with no shock system formed. The mixing layer waves up and down with no thourough breakdown. It impinges on the rear wall of the cavity. The interaction between the shear layer and the aft wall gives rise of two consequences. First, a recirculation flow is formed in the cavity due to the entrainment of the shear layer and the flow reverse after the impingement below the rear wall. Second, the interaction provides an effective feedback that amplifies the shear layer instability. It is shown that the impingement of the shear layer on the cavity aft wall alters the intensity and the extension of the recirculation bubble, which interacts with the mixing layer and consequently provides the amplification condition for this instability. The shear-layer instability is coupled with the pressure waves generated in the cavity and producing acoustic tones at discrete frequencies as analyzed in Section 3.1.2. Moreover, the flow exhibits significant time-dependent three-dimensionality, as can be seen from the flow motions on the zoy-section at $x = L/2$. The recirculation bubble evolves not only in the longitudinal streamwise direction, but also presents vortical motions in the transverse spanwise direction.

In Figure 3.11 the three-dimensional vortical motion has been further illustrated by plotting the unsteady velocity fields at an arbitrary time instant t_0 on different zoy-planes perpendicular to the streamwise direction (i.e. snapshots at t_0 on different x/L stations). The recirculating motion is contained within the cavity in the front part, where the vortical motion is close to the mixing layer and is relatively weak with a low level of turbulence intensity. At and after the mid-section of the cavity (i.e. for $x/L \geq 0.50$), the motion becomes intensified and extended to the cavity floor, forming two counter-rotating re-

circulation bubbles. In the downstream part of the cavity, the vortical motion becomes more extensive and raises to the cavity opening, inducing secondary vortical flow motions above the edges of the cavity side walls. The prediction discloses that the mixing layer, together with the side-walls, brings up vortices. Moving downstream, the vortex is detached from the side-wall edge and being stretched, which is further evolved into the large vortical motion near the opposite side wall. These relatively large vortices are raised up gradually, when moving downstream, and are merged into the freestream, prior to the impact with the aft edge of the cavity. Over the side-wall edges instantaneous mass injection and removal have taken place by the stretching of vortices, similar to the mass exchange process occurring over the aft edge of the cavity. These vortical motions are closely coupled with the pressure oscillations inside the cavity in terms of the pressure modes and their resonant frequencies.

In Figure 3.12, the time-averaged mean flow field is illustrated on the same yz-planes as in Figure 3.11, which have been contoured with the mean streamwise vorticity, Ω_x. The mean flow field is symmetric about the mid-section $z = 0$. After about one-third of the cavity length from the cavity front wall, a pair of anti-recirculating bubbles are formed and sustained by the side walls and become more intensified in the downstream. Unlike in the unsteady motion, only mass removal is observed in the mean flow motion through the cavity side-wall edges. The mass injection into the cavity is accomplished through the center of the cavity opening due to the two symmetric recirculating motions. The mean flow recirculation bubbles are formed on the edge of the side walls, shortly after the mixing layer is released from the leading edge of the cavity (e.g. at $x/L = 0.3$ in Figure 3.12 (b)). The bubbles are elongated towards the cavity floor and becoming more intensive at about the mid-length of the cavity (e.g. at $x/L = 0.5$ in Figure 3.12 (d)). Moving further downstream, the recirculation bubbles start raising gradually. As the cavity aft wall is approached (e.g. at $x/L = 0.9$ in Figure 3.12 (h)), the bubbles are raised up over the cavity opening and are merged into the freestream flow, while the secondary bubbles formed in the corners below the side-walls become sensibly extensive and have helped to lift the two large bubbles out of the cavity.

In Figure 3.13, the mean $w - v$ velocity field is further demonstrated at the section $x/L = 0.5$, accompanied with the contour of the streamwise vorticity component, Ω_x. It is shown that the recirculating motions on each side of the mid-section ($z = 0$) have opposite directions (opposite signs to Ω_x). It should be noted that the mean flow field should be symmetric about $z = 0$, since the geometry and flow conditions are symmetric. The symmetry has been preserved in general, but slightly biased flow features can be observed. Particularly, in the region near the cavity front wall, where the flow motion is relatively slow with a large time scale. To reach statistically independent flow field, a very long time period is required for time-averaging, for which it has taken more than $50T_0$ in the present computation. This averaging time should have effectively smoothed the effect of unsteadiness on the mean flow properties.

In order to highlight the details of the mean flow for the shear layer over the cavity opening, the velocity field and the streamlines are plotted on the mid-section at $z = 0$ in Figure 3.14, where the velocity is colored with the mean turbulent eddy viscosity, while the streamlines are colored with the mean pressure coefficient. As shown, recirculating motion is formed under the shear layer in the cavity with a very small secondary bubble in the lower corner of the front wall. The shear layer tends to be deflected and to attach toward the cavity floor at about $x/L = 0.8$. Consequently, the recirculation tends to be separated with a large bubble in the front part of the cavity and a small bubble in the rear part in front of the cavity aft wall. This implies that the momentum in the

shear layer has to some extent been decayed and is not able to bring the *whole* mixing layer toward and impinge on the cavity rear wall. Instead, a part of the flow is separated from the mixing layer and evolves into the large recirculation bubble and reattaching toward the cavity floor. The rest of the mixing layer approaches the rear wall and impinges on it, causing the small recirculation bubble and large surface pressures. These predicted features may be attributed to two plausible reasons. First, the pressure wave propagating upstream is too intensive, which has damped the strength of the shear layer. Second, the shear layer in the downstream part is too diffusive, because of a too large turbulent eddy viscosity. Such flow phenomena have consequently entailed high mean surface pressures, as indicated in 3.14 (b) on the rear wall face and on the cavity floor below the rear wall. The impingement has triggered high pressures on the rear wall surface. The high pressure on the cavity floor has been partly induced by the reattaching tendency of the deflected shear layer at the end of the large bubble, and partly by the insufficient mass exchange between the cavity and the freestream. The mass removal entailed by the mixing layer from the cavity (through the cavity trailing edge) is relatively low (and thus high pressures in the rear part of the cavity). The predicted cavity flow is not a typical, *pure* open cavity flow as described by Tracy et al. [5]. Instead, it possesses also some characteristics of a transitional-open cavity flow. Indeed, the *separating* and *re-reattaching* flow features arising in the conjunction region between the large recirculation bubble and the small separation bubble have brought about a longitudinal pressure gradient, as depicted in Figure 3.9, which is very similar to the pressure distribution for a typical transitional-open cavity flow [5, 6]. The present URANS modelling has pronounced the cavity flow more like a transitional-open cavity type. If this is the case in practice, for example, for embedded weapon bays, a large longitudinal pressure gradient, particularly near the cavity aft wall, may contribute to large nose-up pitching moments that may cause problems for separating store.

In Figure 3.15, the URANS computed mean flow quantities are compared with the LES data by Larcheveque et al. [17]. The vertical profiles have been plotted on the mid-section $z = 0$ at a number of x/L-stations between the front and aft cavity walls. It is shown that, in general, the predicted streamwise velocities are in good agreement with the LES data, particularly, in the region for $x/L < 0.5$ where the shear layer has been well captured, as shown in Figure 3.15 (a). When approaching the rear wall face for $x/L > 0.8$, reasonable agreement for the streamwise velocities is produced between the URANS result and the LES data. Discrepancies arise in the region where a part of flow is separated from the shear layer and evolving into the recirculation region and tending to separate the cavity into two recirculating zones. This has made the streamwise velocity on the inner edge of the mixing layer somewhat over-predicted. As shown in Figure 3.14, the flow in this region undergoes extensive flow deformation with strong streamline curvature. A linear RANS model, such as the S-A model, may not be appropriate enough to represent the underlying intricate flow physics in this region. Moreover, the present grid resolution seems not sufficient to resolve the shear layer, as reflected also in 3.15 (b), where the turbulent shear stress has been predicted with relatively large discrepancies in the shear layer, in particular above the cavity opening ($y/D > 0$) and in the recirculation region for $0.5 \leq x/L < 0.8$. Further investigation should be undertaken using a RANS model with curvature corrections on a sufficiently refined mesh cross the mixing layer and for the downstream part of the cavity.

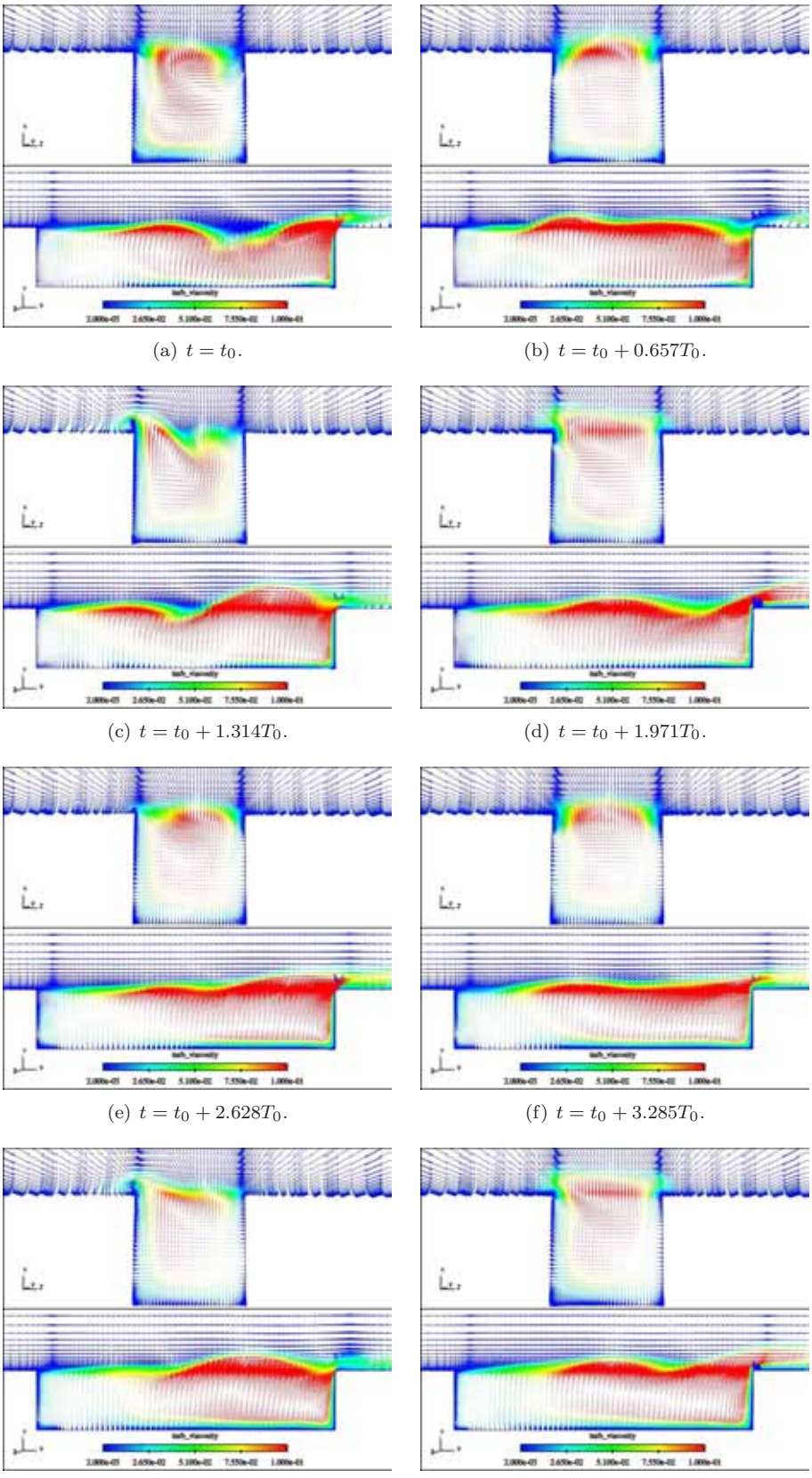

(a) $t = t_0$.

(b) $t = t_0 + 0.657T_0$.

(c) $t = t_0 + 1.314T_0$.

(d) $t = t_0 + 1.971T_0$.

(e) $t = t_0 + 2.628T_0$.

(f) $t = t_0 + 3.285T_0$.

(g) $t = t_0 + 3.942T_0$.

(h) $t = t_0 + 4.600T_0$.

Figure 3.10: Computed unsteady flow fields at different times at sections $x = L/2$ (upper) and $z = 0$ (lower). The time scale $T_0 = L/U_\infty$.

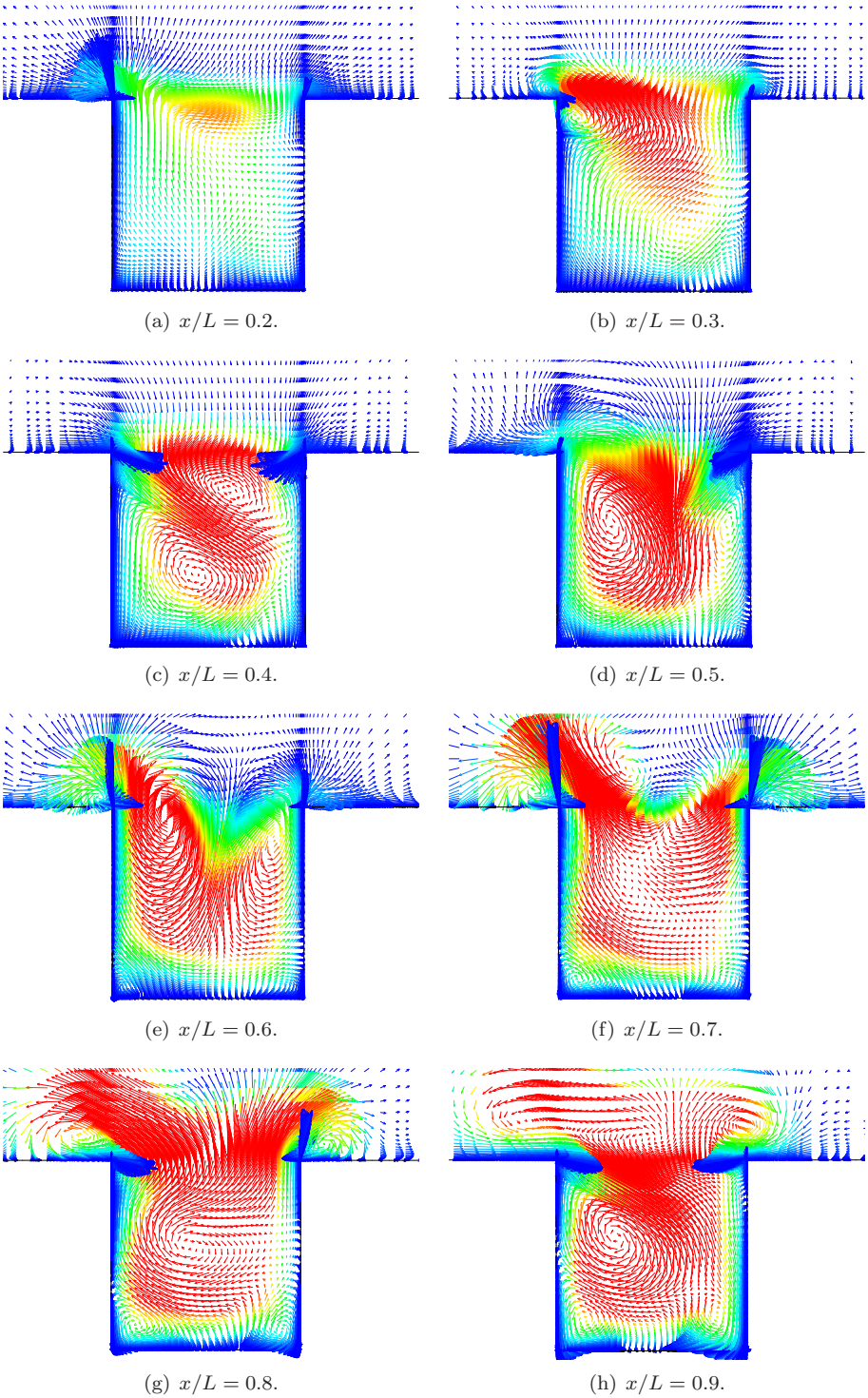

(a) $x/L = 0.2$. (b) $x/L = 0.3$.

(c) $x/L = 0.4$. (d) $x/L = 0.5$.

(e) $x/L = 0.6$. (f) $x/L = 0.7$.

(g) $x/L = 0.8$. (h) $x/L = 0.9$.

Figure 3.11: Unsteady $w - v$ velocity fields at an arbitrary time instant t_0, illustrated on different zoy-planes. Colored with eddy viscosity, same legend as in Fig. 3.10.

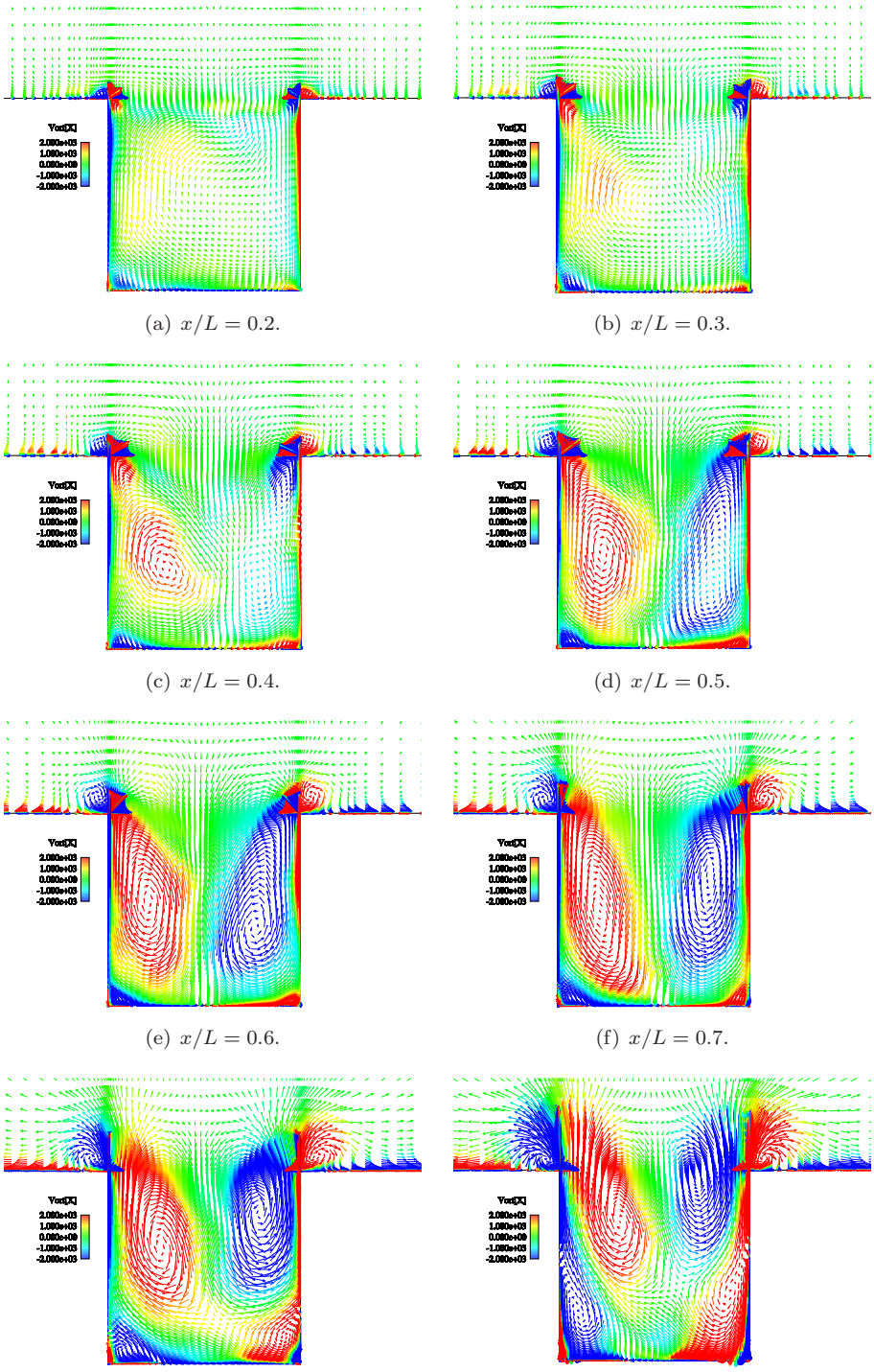

(a) $x/L = 0.2$. (b) $x/L = 0.3$.

(c) $x/L = 0.4$. (d) $x/L = 0.5$.

(e) $x/L = 0.6$. (f) $x/L = 0.7$.

(g) $x/L = 0.8$. (h) $x/L = 0.9$.

Figure 3.12: Mean $w - v$ velocity fields on different zoy-planes, contoured with the mean streamwise vorticity, Ω_x.

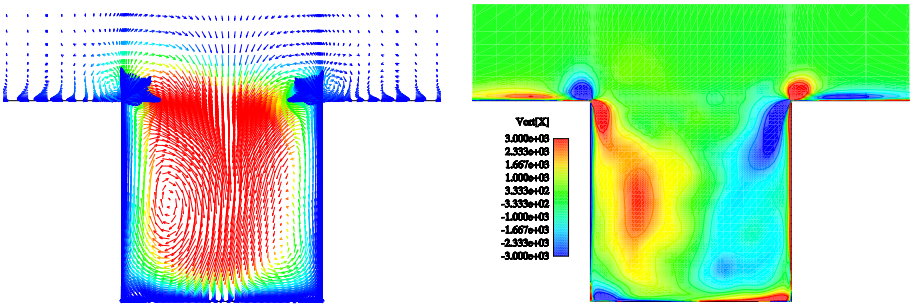

(a) Mean $w - v$ velocity field. (b) Mean vorticity component,Ω_x.

Figure 3.13: Mean flow on the zoy plane at $x/L = 0.5$. (a). $w - v$ velocity field colored with mean eddy viscosity, same legend as in Fig. 3.10. (b) Vorticity component in the x-direction, Ω_x.

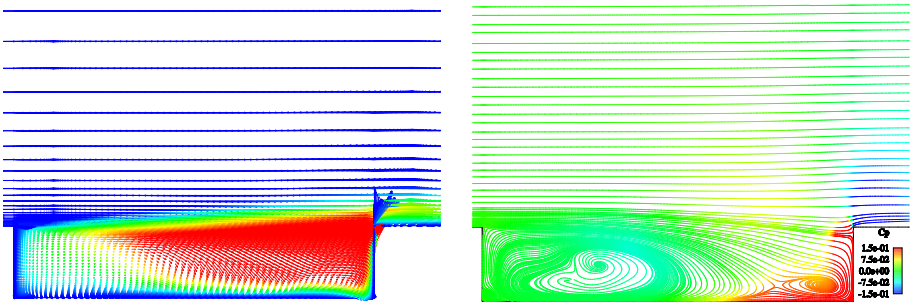

(a) $u - v$ velocity field. (b) Illustration of streamlines.

Figure 3.14: Mean flow on the mid-section at $z = 0$. (a) $u - v$ velocity field colored with mean eddy viscosity, same legend as in Fig. 3.10. (b) Streamlines colored with the pressure coefficient.

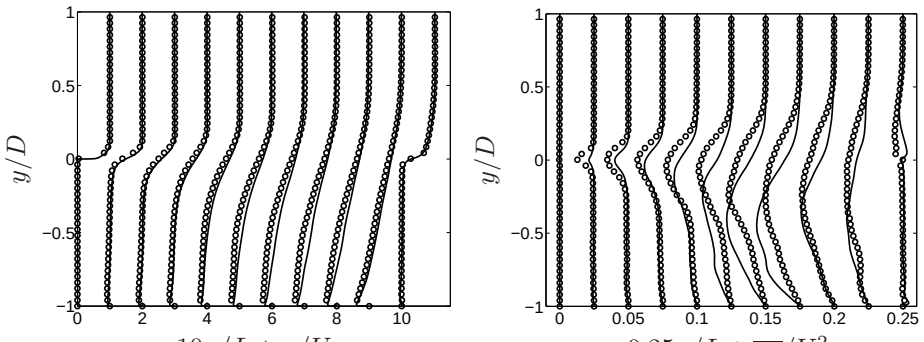

(a) Mean streamwise velocity. (b) Turbulent shear stress.

Figure 3.15: Mean streamwise velocity and turbulent shear stress on the mid-section, $z = 0$, in comparison with full-resolved LES data at stations, from left to right, $x/L = 0, 0.1, 0.2, 0.3, 0.4, 0.5, 0.6, 0.7, 0.8, 0.9$ and 0.997.

4 Conclusions

An unsteady RANS computation has been performed for the turbulent flow over a weapon-bay cavity. The cavity has an aspect ratio of 5 : 1 : 1. The Spalart-Allmaras one-equation RANS model has been employed to model the turbulence effect. The open-cavity geometry, embedded in a flat plane, is simplified from a weapon-bay configuration at a freestream Mach number of $M_\infty = 0.85$. The main focus is on the prediction of the surface pressure fluctuations and resulting sound resonance, as well as on the predicted cavity flow features, in comparison with available experimental measurements (for pressure fluctuations) and with full-resolved LES data (for the mean flow).

For the pressure oscillations over the cavity floor surface, the present 3D URANS modelling has obviously improved the prediction over previous 2D URANS simulations. Nevertheless, it is shown that the 3D URANS computation has to some extent over-predicted the pressure fluctuations, as compared with the experimental measurement, but has reproduced the tendency as observed experimentally with an increasing longitudinal distribution of P_{rms}. In the analysis of sound resonance due to cavity pressure fluctuations, it is shown that the four typical Rossiter tonal modes observed in the experiment are somewhat numerically traceable in the pressure spectra from URANS computations. The spectra peaks at some locations for the first and forth modes become somewhat smeared out and not so verifiable, however. The predicted second and third tonal modes, which are dominant ones, are in general distinguishable from the computed pressure spectra, although the third mode becomes less sensible at the location on the cavity floor towards which the predicted mixing layer is deflected. In general, the frequency for the third mode has been well reproduced, while the frequency to the the second mode is somewhat overestimated. The first and the forth tonal modes computed from the URANS modelling may become hardly visible at some locations. The frequency of the first mode is over-predicted, as compared with the measured one. Corresponding to the over-predicted magnitude for the pressure fluctuations, the amplitudes of PSD and SPL have been somewhat overestimated by the URANS modelling. The over-prediction of the pressure fluctuations may be attributed to the insufficient mass removal from the cavity through the cavity trailing edge. This implies that the URANS modelling has under-estimated the intensity of the mixing layer in the downstream part when approaching the aft cavity wall. In addition, it is noted that the simulation indicates large mean pressures and pressure fluctuations near and on the cavity rear wall, where potential structural fatigue may arise.

Unlike 2D cavity flows, the unsteady 3D flow field obtained from the present URANS modelling does not exhibit obvious periodic flow features. Nonetheless, it is shown that the flow oscillation has been mainly manifested by the instability of the shear layer with enriched turbulence. The shear layer *waves* up and down, showing instant tendency of mixing-layer breakdown. The shear layer travels over the cavity and, consequently, impinging on the rear cavity wall. Prior to the impingement, on the other hand, a part of the flow has

separated/deflected from the shear layer and involved into the recirculation bubble with a tendency of being attached towards the cavity floor. Along with some flow features arising usually from open-cavity flows, the predicted mean static pressure distribution along the cavity floor is similar to that for a transitional-open cavity flow, which presents a large, undesirable longitudinal pressure gradient in the rear part of the cavity (particularly near the rear wall). This is consistent with the prediction of the mean flow field in this region where the mixing layer is deflected toward the cavity floor. Moreover, the analysis of the flow field shows that the flow consists of counter-recirculating vortical motions in the cavity with fairly extensive streamwise vorticity components. Moving from the front to the aft cavity wall, these vortical motions become intensified and arise to the cavity opening, entailing vortices on the edge of cavity side walls. As compared with the LES data, it is shown that the prediction of the mean streamwise velocity is reasonable, but the computed turbulent shear stress presents sensible discrepancies, particularly, in the recirculating region after the upstream half-length of the cavity. This may partly be attributed to the incapability of a linear one-equation turbulence model in dealing with the highly anisotropic flow features. On the other hand, the mesh resolution gridded in the cavity and over the mixing layer needs to be further verified and refined in 3D simulations, which may impose effects on the prediction in the downstream part of the cavity. Moreover, it should be noted that the present 3D URANS results have shown significant improvement over previous simulations for a 2D cavity configuration. In parallel to the 3D URANS simulation, a DES computation has been performed for the same cavity flow with the same mesh [14]. It is shown that the DES enables extensively enriched vortical motions in the cavity, yet calls for refined mesh resolution for the shear layer.

Acknowledgments

The LES data was kindly provided by Dr L. Larcheveque and Prof P. Saugaut at Universite Paris VI.

Bibliography

[1] A. Roshko. Some measurements of flows in a rectangular cutout. NACA TN 3488, 1955.

[2] T. Colonius. An overview of simulation, modeling, and active control of flow/acoustic resonance in open cavities. AIAA Paper 2001-0076, 2001.

[3] R. L. Stallings and D. K. Forrest. Separation characteristics of internally carried stores at supersonic speeds. NASA TP-2993, 1990.

[4] F. J. Wilcox. Experimental measurements of internal store separation characteristics at supersonic speeds. Store Carriage, Integration and Release, Royal Aeronautical Society, pp.5.1-5.16, 1990.

[5] M. B. Tracy and E. B. Plentovich. Characterization of cavity flow field using pressure data obtained in the Langley 0.3-meter transonic Cryogenic tunnel. NASA Tech. Memorandum 4436, 1993.

[6] S. M. Grace. An overview of computational aeroacoustic techniques applied to cavity noise prediction. AIAA 2001-0510, 2001.

[7] V. Sarohia. *Experimental and analytical investigation of oscillations in flows over cavities*. PhD thesis, California Institute of Technology, USA, 1975.

[8] C. W. Rowley, T. Colonius, and A. J. Basu. On self-sustained oscillations in two-dimensional compressible flow over rectangular cavities. *Journal of Fluid Mechanics*, 455:315–346, 2002.

[9] J. E. Rossiter. Wind tunnel experiments on the flow over rectangular cavities at subsonic and transonic speeds. Rep. Mem. 3438, Aeronautical Research Council, 1964.

[10] S. Srinivasan and O. Baysal. Navier-Stokes calculations of transonic flow past cavities. *Journal of Fluid Engineering*, 113:369–376, 1991.

[11] C.-J. Tam, P. D. Orkwis, and P. J. Disimile. Algebraic turbulence model simulations of supersonic open-cavity flow physics. *AIAA Journal*, 34:2255–2260, 1996.

[12] S. T. Shih and P. J. Morris. Parallel computational aeroacoustic simulation of turbulent subsonic cavity flows. AIAA Paper 2000-1914, 2000.

[13] S.-H. Peng. Unsteady RANS simulation of turbulent cavity flow: Summary of 2D baseline computations. FOI-R-1915-SE, Systems Technology, Swedish Defence Research Agency, Stockholm, 2006.

[14] S.-H. Peng. Simulation of flow past a rectangular open cavity using DES and unsteady RANS. AIAA Paper 2006-2827, San Francisco, 2006.

[15] M. J. Stanek, G. Raman, V. Kibens, J. A. Ross, J. Odedra, and J. W. Peto. Control of cavity resonance through very high frequency forcing. AIAA Paper 2000-1905, 2000.

[16] M. J. Stanek, G. Raman, V. Kibens, J. A. Ross, J. Odedra, and J. W. Peto. Supression of cavity resonance using high frequency forceing- the characteristic signature of effective devices. AIAA Paper 2001-2128, 2001.

[17] L. Larcheveque, P. Sagaut, T.-H. Le, and P. Comte. Large eddy simulation of a compressible flow in a three-dimensional open cavity at high reynolds number. *J. Fluid Mech.*, 516:265–301, 2004.

[18] P. Eliasson. EDGE: A Navier-Stokes solver for unstructured grids. FOI-R-0298-SE, FFA, Swedish Defence Research Agency, Stockholm, 2001.

[19] C. Hirsch. *Numerical Computation of Internal and Externa Flows*. Vol. 1, John Wiley & Sons, Interscience Publication, 1989.

[20] P. R. Spalart and S. R. Allmaras. A one-equation turbulence model for aerodynamic flows. AIAA Paper 92-0439, Reno, 1992.

[21] L. Martinelli. *Calculation of Viscous Flows with Multigrid Methods*. PhD thesis, Department of Mechanical and Aerospace Engineering, Princeton University, Princeton, 1987.

[22] A. Jameson. Time dependent calculations using multigrid, with applications to unsteady flows past airfoils and wings. AIAA Paper 91-1596, AIAA 10th Computational Fluid Dynamics Conference, 1991.

[23] R. M. Ashworth. TurMMAC weapon bay application chanllenge- final analysis. Rept. TFD/94/10, QinetiQ/FST/AVS/TR046679, 2004.

[24] D. Rockwell and E. Naudascher. Review-self-sustaining ocillations of flow past cavities. *Journal of Fluid Engineering*, 100:152–165, 1978.

FOI is an assignment-based authority under the Ministry of Defence. The core activities are research, method and technology development, as well as studies for the use of defence and security. The organization employs around 1350 people of whom around 950 are researchers. This makes FOI the largest research institute in Sweden. FOI provides its customers with leading expertise in a large number of fields such as security-policy studies and analyses in defence and security, assessment of different types of threats, systems for control and management of crises, protection against and management of hazardous substances, IT-security an the potential of new sensors.

FOI
Swedish Defence Research Agency
SE-164 90 STOCKHOLM

Tel: +46 8 5550 3000
Fax: +46 8 5550 3100

www.foi.se